Magnetism of solids resulting from spin polarization of p orbitals

2010 J. Phys.: Condens. Matter 22 073202

(http://iopscience.iop.org/0953-8984/22/7/073202)

IOP PUBLISHING JOURNAL OF PHYSICS: CONDENSED MATTER

J. Phys.: Condens. Matter **22** (2010) 073202 (19pp) doi:10.1088/0953-8984/22/7/073202

TOPICAL REVIEW

Magnetism of solids resulting from spin polarization of p orbitals

O Volnianska[1] **and P Boguslawski**[1,2]

[1] Institute of Physics PAS, aleja Lotnikow 32/46, PL-02-668 Warsaw, Poland
[2] Department of Mathematics, Physics and Technology, University of Bydgoszcz, ulica Chodkiewicza 30, PL-85-064 Bydgoszcz, Poland

Received 16 November 2009, in final form 20 December 2009
Published 2 February 2010
Online at stacks.iop.org/JPhysCM/22/073202

Abstract
Magnetism in systems that do not contain transition metal or rare earth ions was recently observed or predicted to exist in a wide variety of systems. We summarize both experimental and theoretical results obtained for ideal bulk II–V and II–IV compounds, molecular crystals containing O_2 or N_2 molecules as structural units, as well as for carbon-based materials such as graphite and graphene nanoribbons. Magnetism can be an intrinsic property of a perfect crystal, or it can be induced by non-magnetic dopants or defects. In the case of vacancies, spin polarization is local and results in their high spin states. The non-vanishing spin polarization is shown to originate in the strong spin polarization of the 2p shell of light atoms from the second row of the periodic table.

(Some figures in this article are in colour only in the electronic version)

Contents

1. Introduction

This review is devoted to magnetism in systems that do not contain transition metal or rare earth ions with partially filled d or f shells. In recent years, magnetism based on s and p electrons only was experimentally discovered and/or theoretically predicted to exist in a number of cases. Our goal is to summarize both experimental and theoretical results, and highlight mechanisms responsible for the non-vanishing spin polarization. The systems analysed thus far differ in their nature, i.e. in crystal structure, chemical composition and type of magnetic properties.

Atomic spin polarization of p orbitals is the strongest for light atoms from the second row of the periodic table, for which the Hund energy is close to that of transition metal atoms. This explains why only crystals that contain C, N and O are expected, and found, to be spin-polarized. This basic fact provides a common denominator for all systems included here. As in the case of d or f shells, in order to carry spin moment the p shell must be partly occupied. Typically this is not the case. Partial occupation is much easier to achieve for the d shell of transition metal ions. They possess outer s valence electrons that shield the d electrons by forming bonds with neighbours, leaving d electrons weakly hybridized, which allows for an efficient atomic-like intra-shell exchange interaction in a crystal. The valence p shell of ions in a solid as a rule is fully occupied with electrons that form bonds, acquiring a closed-shell configuration with vanishing spin. Partial occupation can be achieved by choosing a proper stoichiometry of an ideal crystal, as in II–V and II–IV compounds or molecular crystals discussed here. Alternatively,

empty p states, or p (or sp^n) dangling bonds, exist at surfaces, nanoribbon edges or at planar or point defects in the bulk. Similarly, light impurities may form spin-polarized bands in semiconductors. In the case of defects or dopants, spin polarization depends on their charge state which is determined by the Fermi energy and thus, for example, the presence of compensating native defects.

This review begins with ideal crystals. In particular, the non-vanishing spin polarization of II^A-N nitrides and II^A–IV carbides discussed in section 2 stems from the fact that light anions provide localized spin moments and, due to the stoichiometry and crystal structure of this family, those compounds are metals. Thus, the Zener-like mechanism of magnetism is operative. The question regarding the stability of these open-shell structures relative to the closed-shell insulating and non-magnetic ones is also addressed.

Magnetic properties of molecular crystals such as Rb_4O_6 are reviewed in section 3. In this case magnetic moments are localized on O_2 dimers, or more specifically on the $\pi^*(O_2)$ molecular antibonding orbitals with two electrons in the high spin configuration that is not destroyed by hybridization with neighbours in a solid. This class of materials exhibits antiferromagnetism.

Section 4 is devoted to the magnetism of non-magnetic crystals that contain defects or non-magnetic impurities. In particular, *local* magnetization of vacancies in the high spin state is attracting a considerable amount of attention. Typically, defects in semiconductors assume low spin configurations, with total spin $S = 0$ or $1/2$. High spin states of vacancies with $S = 1$ or $3/2$ were observed in several semiconductors four decades ago, but the effect was explained only recently. This effect leads to a premise that vacancies or dopants at sufficiently high concentrations can lead to a macroscopic magnetization of a sample. Indeed, ferromagnetism of, for example, ZnO doped with C was discovered. Here again both local and global spin polarization follows from the presence of partially occupied p orbitals of light atoms.

Defects are also responsible for the observed magnetism in various forms of carbon. These include graphite and nanographite irradiated or implanted with various species, as summarized in section 5. The defects may be point or planar, but in both cases the non-saturated broken bonds of carbon are at the origin of the magnetic properties. Graphene belongs to this family as well, but, given the amount of work currently devoted to nanoribbons, it constitutes a target *per se*. Spin polarization is related to a particular topology of ribbon edges, and thus is intrinsic to graphene and affects its electronic structure. An overview of pertinent results is given in section 6, closing this review.

Finally, in some cases, which are not mentioned here, the observed ferromagnetism turned out to result from the presence of magnetic contamination such as Fe ions in the samples. This critical issue is now thoroughly controlled, and those past results serve as warnings for current researchers and readers.

2. Ideal bulk systems: II^A–V and II^A–IV compounds

Recently, several II^A–V and II^A–IV compounds without transition metals were predicted to be half-metals with a total spin polarization of holes in the valence band [1–10]. The calculations were typically based on the local spin density approximation (LSDA) and/or generalized gradient approximation (GGA). Zinc blende (zb), rock salt (rs) and NiAs crystal structures were considered. The stability of the spin-polarized ferromagnetic (FM) case relative to the non-polarized (PM) situation is given by the energy difference $\Delta E^{\mathrm{FM-PM}} = E^{\mathrm{FM}} - E^{\mathrm{PM}}$.

Table 2.1. Energies of spin polarization $\Delta E^{\mathrm{FM-PM}}$ (in meV per two atoms) for rs, NiAs and zb structures. The last column gives energies of spin polarization of isolated group-V atoms (in eV) [4].

	$\Delta E^{\mathrm{FM-PM}}$ (crystal)			
	rs	NiAs	zb	$\Delta E^{\mathrm{FM-PM}}$ (anion)
BaN	−90	−105	−125	
SrN	−135	−205	−185	
CaN	−140	−125	−195	−2.45
CaP	−3	0	−55	−1.37
CaAs	0	0	−40	−1.24
CaSb	0	0	−5	−1.02

We begin with II^A–V crystals. The results obtained in [4] are summarized in table 2.1. Spin polarization of the considered compounds in the zb structure is non-vanishing, and the calculated magnetic moment per unit cell is 1 μ_B (this also holds for other spin-polarized structures). On the other hand, zb–MgP, zb–MgAs and all zb–Be–V crystals are paramagnetic, i.e. $\Delta E^{\mathrm{FM-PM}} = 0$.

To understand the calculated magnetic properties one may follow the formation of an II^A–V crystal in a wide range of lattice parameters a, ending with the case of a compressed solid. Total energies and magnetic moments of zb and rs–CaN are shown in figure 2.1. These and other results shown in the following are typical for other II^A–V compounds. One may see that there are three ranges of lattice constants characterized by qualitatively different properties, for which the magnetic moment per unit cell is 3, 1 and 0 μ_B, and which are denoted as A, B and C, respectively. In the case of large lattice parameters, i.e. of 'isolated atoms', the total magnetic moment is the superposition of the magnetic moments of Ca (=0) and N (=3 μ_B). With the decreasing lattice spacing the atoms begin to interact and form bonds. Figure 2.1 shows that the onset of formation of bonds (displayed by the decrease of total energy) is correlated with the drop of magnetization, which occurs at ∼9 Å for zb–CaN and ∼8.5 Å for rs–CaN. The magnetic moment is then constant for 4.5 Å $< a <$ 9 Å for the zb or 3.7 Å $< a <$ 8.5 Å for the rs phase, respectively.

The origin of ferromagnetism found for several II^A–V and II^A–IV crystals was identified by analysing their electronic structure [4]. The emerging picture is particularly clear for the zinc blende phase. Considering the series of Ca compounds (CaN, CaP, CaAs, CaSb) one can see from figure 2.2 that $\Delta E^{\mathrm{FM-PM}}$ is the largest for CaN, −195 meV, it decreases with the increasing atomic number of the anion, and it almost vanishes for CaSb. This suggests that anions play a dominant role in determining spin polarization. In fact, as clearly follows from figure 2.2, the above trend fully correlates with the trend exhibited by the calculated energies of spin polarization

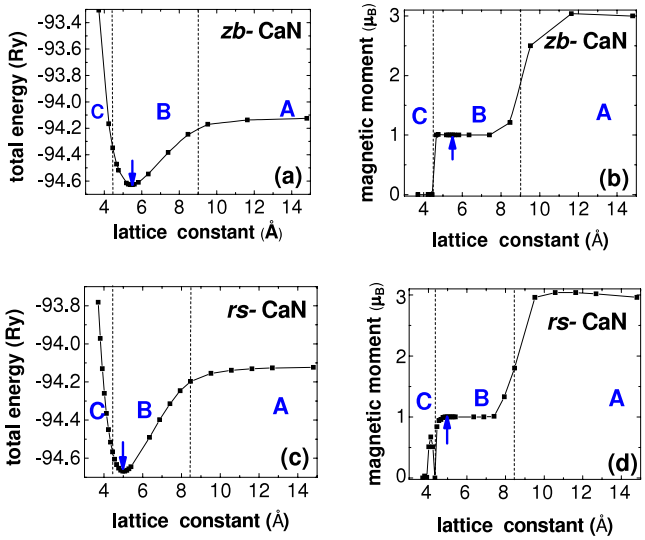

Figure 2.1. Total energy ((a), (c)) and total magnetic moment per unit cell ((b), (d)) as a function of the lattice constant of CaN. Arrows indicate the equilibrium lattice constant a_{eq}. Reproduced with permission from [4]. Copyright 2007 by the American Physical Society.

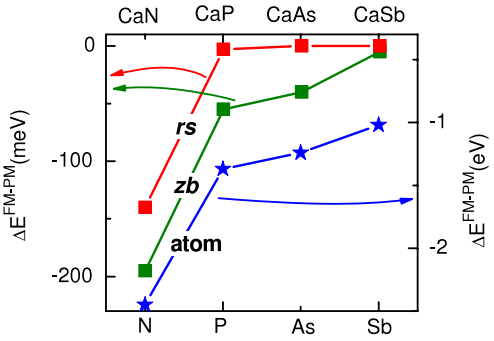

Figure 2.2. Difference in energies of FM and PM phases $\Delta E^{\mathrm{FM-PM}}$ for CaX compounds in the rs and zb structures, together with those for isolated anions. The lines are to guide the eyes. Reproduced with permission from [4]. Copyright 2007 by the American Physical Society.

of isolated anions, which decrease from −2.45 eV for N to −1.02 eV for Sb. Moreover, the spin polarization energy of N is about twice as high as for the remaining anions. This fact explains the pronounced stabilization of spin polarization found for zb, rs and NiAs structures of the nitrides. In other words, the driving force of ferromagnetism is the spin polarization of partially occupied p(N) orbitals. The effect follows from the compactness of p orbitals of N, as well as those of C, O and S, relevant for other systems considered here. The radii of these orbitals shown in figure 2.3 and their Hund energies are close to those of the d electrons of Mn.

This hypothesis is confirmed by the analysis of the density of states (DOS) and of the projection of the wavefunction on atomic orbitals shown in figure 2.4 for rs–CaN. One can see that the states of majority-spin electrons are filled. For the minority-spin channel the Fermi level E_{F} crosses the valence band. The top of the valence band is mainly formed from the p

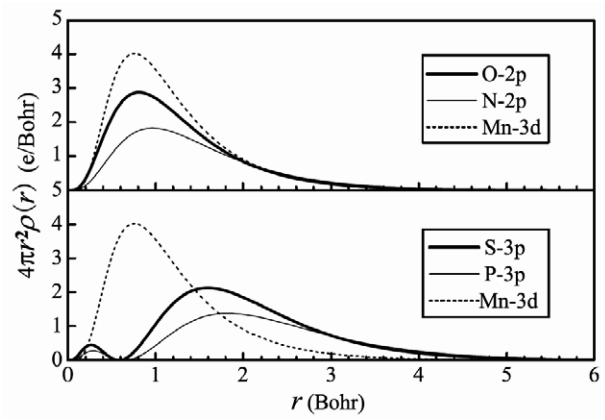

Figure 2.3. Radial charge distribution, $4\pi r^2\rho(r)$, for N, O, P and S valence p orbitals as well as for Mn d orbitals. Reproduced with permission from [11]. Copyright 2009 by the American Physical Society.

orbitals of N, which contribute about 75%. The contribution of d orbitals of cations to the valence bands is at least five times smaller; these orbitals (which are the lowest *excited* states of cations) contribute mainly to the conduction states.

The contour plots of the spin density displayed in figure 2.5 for both zb– and rs–CaN confirm the conclusion that the spin polarization of crystals results from the spin polarization of the p (anion) states. In accord with figure 2.4, the contribution of Ca states is visible, but small. Qualitatively identical results are obtained for BaN and SrN. Finally, we note that a large contribution of the d(Ca) states to the valence bands could in principle explain the magnetism of $\mathrm{II^A}$–V compounds. However, the obtained results show that this is not the case.

Analysis of the energy bands shows that $\mathrm{II^A}$–V compounds in both zb and rs structures are half-metals, i.e. holes at the Fermi level are fully spin-polarized. Their metallic character is due to the fact that they have seven valence electrons, i.e. one free hole, per unit cell. The weak dispersions and somewhat atypical shapes of the upper valence bands result mainly from the large values of the lattice constant due to the large atomic radii of cations [4].

Formation of FM was also predicted for $\mathrm{II^A}$–IV compounds. The DOS for rs–SrC, shown in figure 2.6, displays the dominant contribution of spin-polarized p(C) orbitals, thus demonstrating that the origin of magnetism in $\mathrm{II^A}$–V and $\mathrm{II^A}$–IV compounds is the same.

The relative stability of FM and antiferromagnetic (AFM) phases was analysed in [4]. The calculations were performed only for the most interesting case of rs and zb phases of $\mathrm{II^A}$-N nitrides. The type-I AFM ordering was considered, in which spins of the anions in every (001) plane are parallel, but the sign of the polarization of consecutive planes alternates.[3] The calculated differences between energies of FM and AFM phases, $\Delta E^{\mathrm{FM-AFM}}$, are −5, −35 and −55 meV for rs BaN, SrN and CaN, respectively. This result confirms that

[3] We do not consider other AFM phases since, for example, in zb–MnTe the energies of type-I and type-III AFM orders differ by 2 meV/atom only, see [12]. Similar results are expected for II–V compounds. This value is an order of magnitude smaller than $\Delta E^{\mathrm{FM-AFM}}$ for CaN and SrN and thus does not affect our conclusions.

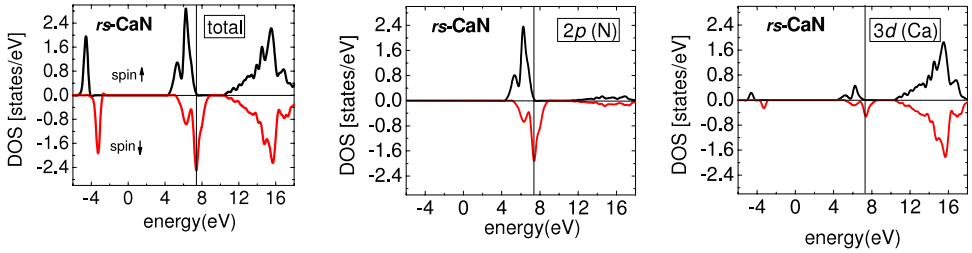

Figure 2.4. Total density of states (a) per unit cell of rs–CaN, and the contributions of (b) p(N) and (c) d(Ca) orbitals. Vertical lines show the Fermi energy. Positive and negative values of DOS hold for spin-up and spin-down states, respectively. Reproduced with permission from [4]. Copyright 2007 by the American Physical Society.

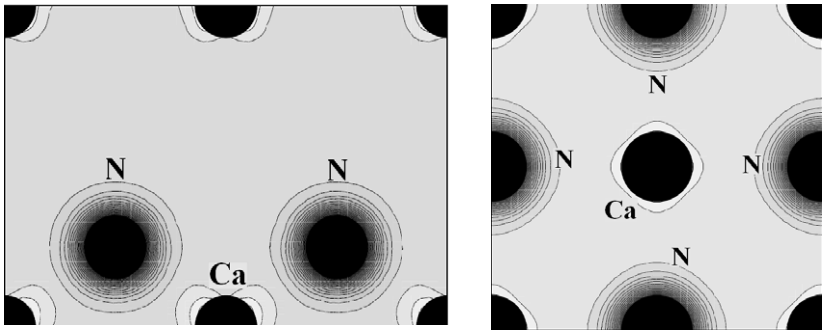

Figure 2.5. Contour plots of the calculated spin density for zb–CaN in the (110) plane (left panel) and rs–CaN in the (001) plane (right panel). Reproduced with permission from [4]. Copyright 2007 by the American Physical Society.

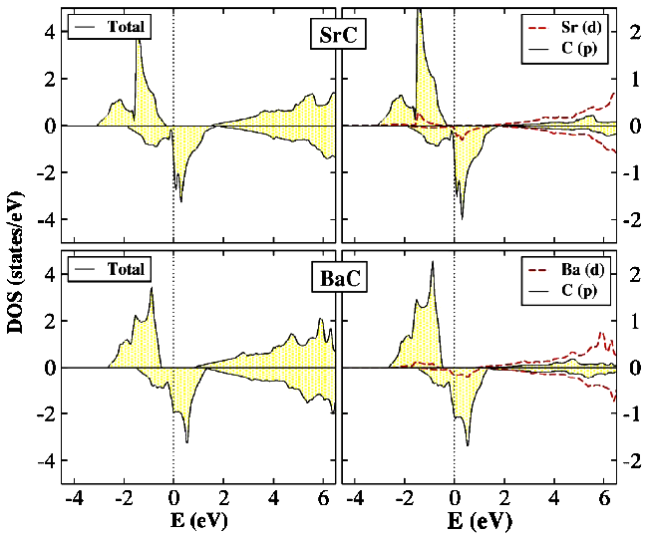

Figure 2.6. Spin-resolved total and partial densities of states for rock salt SrC (upper panel) and BaC (lower panel) at equilibrium lattice constants. Reproduced with permission from [7]. Copyright 2007 by the American Institute of Physics.

the magnetic ground state phase is FM. Furthermore, the absolute values of the energy of spin polarization $\Delta E^{\mathrm{FM-PM}}$ are higher than those of $\Delta E^{\mathrm{FM-AFM}}$, which shows that with the increasing temperature spin polarization should vanish as a result of the disordering of the magnetic moments, and not of their disappearance. Finally, regarding $\Delta E^{\mathrm{FM-PM}}$ as a rough estimate of the Curie temperature T_{C} we observe that $\Delta E^{\mathrm{FM-PM}}$ of about 10 meV corresponds to about 100 K. Consequently, one may expect $\mathrm{II^A}$-nitrides in the rs phase to be FM at temperatures of the order of 100 K. More accurate estimates of T_{C} were not performed.

According to the obtained results, rs-$\mathrm{II^A}$-N nitrides are half-metals. Nevertheless, the flatness of the upper valence band may suggest that these systems are magnetic Mott–Hubbard insulators, similar to several transition metal oxides in which strong electron correlations play a critical role. This possibility may be verified by calculations beyond LSDA that uses methods appropriate for highly correlated systems, such as those specified in sections 3 and 4. However, even if this would be the case, the main physical effect on which we focus here, i.e. the magnetism based on partially filled p (and not d or f) atomic shells, would remain valid.

We now turn to the FM-to-PM transition, i.e. to the destabilization of spin polarization that occurs at sufficiently small lattice constants for all the considered compounds. This transition is seen in figure 2.2 for $\mathrm{II^A}$–V crystals (region C). In all cases, the disappearance of the magnetization is not accompanied by major and abrupt changes of the band structure, since the decrease of the lattice constant induces a progressive decrease of the spin splitting and an increase of the width of the valence bands. In fact, independent of the actual origin of spin polarization, the kinetic energy of carriers and its increase with the decreasing atomic volume under hydrostatic pressure always destabilize the FM phase. The pressure-induced disappearance of magnetization can qualitatively be understood based on the Stoner criterion [13], which indicates that the stability of spin polarization is favoured by large

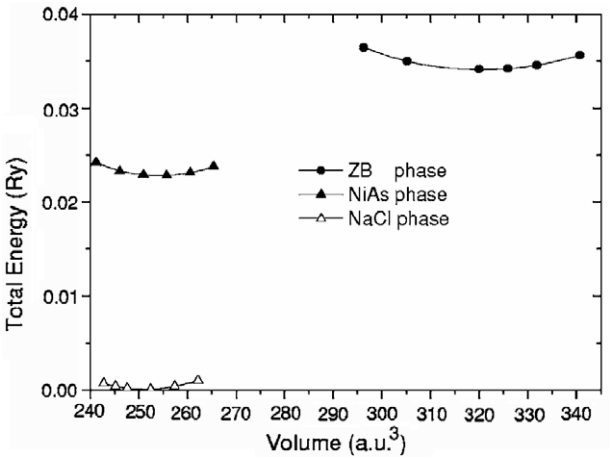

Figure 2.7. Total energy as a function of volume per formula unit for FM CaC in the zb, NiAs and NaCl phases. Reproduced with permission from [6]. Copyright 2007 by the American Physical Society.

magnetic susceptibility, which is proportional to the density of states at the Fermi level, and is destabilized by kinetic energy at high electron densities. These arguments explain the disappearance of the magnetic moment at small lattice constants. More importantly, they highlight the fact that large lattice constants favour spin polarization. This is why, for example, a group II$^{\mathrm{A}}$ cation Ca is 'better' than the corresponding group II$^{\mathrm{B}}$ Zn with a smaller atomic radius, and zb–MgP, zb–MgAs and all zb–Be–V crystals are paramagnetic. The role of kinetic energy is general in character, and to a large degree independent of the crystal structure. In particular, it explains qualitatively the weaker stability of FM in the rs–II$^{\mathrm{A}}$–V crystals, which follows from their equilibrium atomic volumes being smaller by about 15% than in the zb structure.

A problem critical for the synthesis of II-N and II–IV crystals is their equilibrium crystalline structure and the thermodynamically stability. This issue was examined for both II$^{\mathrm{A}}$–V [4] and for II–IV compounds [6–8]. The calculated total energy as a function of the atomic volume for zb, rs and NiAs phases of CaC is presented in figure 2.7, which shows that the most stable phase is rs, while the zb phase is higher in energy. This result characterizes also II$^{\mathrm{A}}$-N nitrides [4], ScN [14] and CaAs [3].

However, the results shown in figure 2.7 do not guarantee thermodynamic stability of the rs phase. Stability of a compound with respect to decomposition into bulk constituents is displayed by its heat of formation, which (at $T = 0$ K) is obtained by considering the reaction to form (or decompose) a crystalline solid from (or into) its components. For bulk II–V nitrides we have

$$\Delta H_{\mathrm{f}} = E_{\mathrm{coh}}^{\mathrm{II-V}} - (n^{\mathrm{II}} E_{\mathrm{coh}}^{\mathrm{II}} + n^{\mathrm{N}} E_{\mathrm{bind}}^{\mathrm{N_2}}/2)/(n^{\mathrm{II}} + n^{\mathrm{V}}), \quad (2.1)$$

where $E_{\mathrm{coh}}^{\mathrm{II-V}}$ and $E_{\mathrm{coh}}^{\mathrm{II}}$ are the cohesive energy per atom of the considered compound and of the group-II metal in its equilibrium structure, respectively, and $E_{\mathrm{bind}}^{\mathrm{N_2}}$ is the binding energy of the N_2 dimer. For other systems analogous expressions hold. Note that, according to this definition, a negative ΔH_{f} implies that the compound is stable against decomposition into bulk constituents. The results for BaN, SrN and CaN show that the Zn_3P_2 structure is more stable than the rs phase because its heat of formation is lower [4]. The calculated difference in ΔH_{f} of Zn_3P_2 and the rs structures is about 0.6 eV/atom. However, we stress that not only the Zn_3P_2 but also the rs phase is thermodynamically stable, which follows from the negative ΔH_{f} of about -0.5 eV/atom. Since the stoichiometries of these structures are different, the formation of one of them should critically depend on the conditions of growth. Consequently, the relative stability of the rs phase of II$^{\mathrm{A}}$–V nitrides justifies the analysis of their magnetic properties. On the other hand, II–V compounds in the zb phase are unstable against decomposition [4].

It should also be stressed that even high cohesive energies do not assess the compound stability. Cohesive energy per two atoms is defined as

$$E_{\mathrm{coh}}^{\mathrm{II-V}} = 2(E_{\mathrm{tot}}^{\mathrm{II-V}} - n^{\mathrm{II}} E_{\mathrm{at}}^{\mathrm{II}} - n^{\mathrm{V}} E_{\mathrm{at}}^{\mathrm{V}})/(n^{\mathrm{II}} + n^{\mathrm{V}}), \quad (2.2)$$

where $E_{\mathrm{tot}}^{\mathrm{II-V}}$ is the total energy per unit cell of the considered compound, E_{at} is the energy of the isolated atom, and n^{II} and n^{V} are the numbers of atoms of groups II and V in the unit cell. Cohesive energies of BaN, SrN and CaN are large (-7.12, -6.78 and -7.48 eV, respectively [4]) which indicates that, after being formed, they are expected to be stable due to the high energies of II-N bonds.

The impact of the spin–orbit coupling on the stability of spin polarization in zb–II$^{\mathrm{A}}$–V compounds was examined in [9]. The authors find that the coupling destroys the polarization for heavier group-V anions, i.e. As, Sb and Bi, but not for the nitrides. The effect is intuitively obvious because the interaction mixes spin-up and spin-down states. One can expect that this conclusion holds also for the nitrides, carbides and oxides in phases other than zb due to the smallness of the spin–orbit coupling of light atoms.

Finally, we comment on the possibility of growing FM II$^{\mathrm{A}}$-N nitrides. In most cases, the Zn_3P_2 phase is more stable than the rs. However, the different stoichiometries of the two phases imply that the formation of the FM rock salt phase should strongly depend on the conditions of growth such as relative flux intensities. Moreover, in epitaxial growth the substrate can determine the structure of the epilayer. Consequently, the choice of appropriate epitaxial conditions should allow obtaining rs–II$^{\mathrm{A}}$–V nitrides. More detailed considerations are given in [4].

3. Ideal bulk systems: molecular magnetism

We now turn to magnetism in ideal bulk crystals that is of molecular rather than atomic origin. This class comprises KO_2, RbO_2, CsO_2, Rb_4O_6, Cs_4O_6 and SrN. The prototype example is solid O_2 [15, 16], which in the two low-temperature phases orders antiferromagnetically at the Néel temperature of about 20 K. With higher pressure the molecular crystal becomes metallic [17] and then superconducting [18]. First observations of magnetic phases in this class of materials were reported in [19] for KO_2, RbO_2 and CsO_2, characterized by a Néel temperature of 7, 15 and 9 K, respectively. The combination

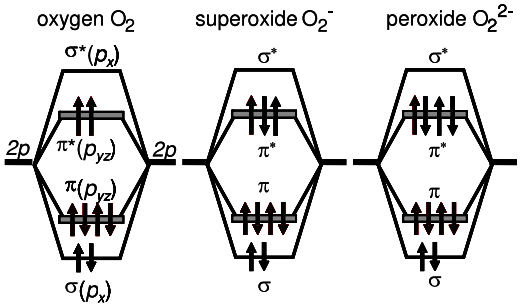

Figure 3.1. Electronic structure of the oxygen molecule (O_2), the superoxide ion (O_2^-) and the peroxide ion (O_2^{2-}). Electronic configuration of N_2^{2-} is the same as that of O_2.

of electron paramagnetic resonance and antiferromagnetic resonance data showed that the easy axis of magnetization is perpendicular to the internuclear axis of the O_2^- ions, and the hard axis is parallel to it for all three compounds. The structural motif common to these systems is the O_2 dimer. In a crystalline phase, O_2 can assume one of three charge states, O_2, O_2^- and O_2^{2-}; their electronic structure is schematically shown in figure 3.1. A neutral O_2 contains two unpaired electrons on the molecular π^* antibonding level. Compactness of p(O) orbitals results in a strong exchange interaction, and the ground state of O_2 is the high spin state with $S = 1$. The superoxide ion has one more electrons on the π^* level and, consequently, the magnetic moment of the ion is reduced to 1 μ_B. Finally, the O_2^{2-} ion occurs in peroxides and its spin moment vanishes.

Molecular magnetism was theoretically predicted [20, 21] and then experimentally observed [22] in rubidium sesquioxide Rb_4O_6. Rb_4O_6 crystallizes in the Pu_2C_3 structure. The unit cell of Rb_4O_6 contains two superoxide O_2^- ions with magnetic moments of about 1 μ_B and four non-magnetic O_2^{2-}, which were identified in inelastic neutron scattering studies [23]. The chemical formula can thus be written as $(Rb^+)_4(O_2^-)_2(O_2^{2-})_4$, and Rb_4O_6 is a molecular mixed-valence compound. Magnetization measurements indicate a magnetic transition at 3.4 K [22]. While theory predicts the effective magnetic moment of 2 μ_B per Rb_4O_6 hyperoxide unit [20, 21], measurements [22] give a lower value 1.83 μ_B; such a discrepancy is acceptable. However, experimentally Rb_4O_6 exhibits a frustrated magnetic order instead of the predicted AFM phase [22]. Magnetization of Rb_4O_6 measured using a superconducting quantum interference device is shown in figure 3.2. One can see that the temperature dependences of the magnetization exhibit hysteresis: the measurements are not reversible if started from a zero-field-cooled state. Irreversibility between the field-cooled and the zero-field-cooled measurements is specific for magnetically frustrated systems such as spin glasses. Investigations were recently extended to Cs_4O_6 [24]; they confirmed the mixed valence character of both Rb_4O_6 and Cs_4O_6. Both compounds exhibit a similar magnetic frustration displayed by time-dependent magnetization, a feature previously known only for d- and f-electron systems.

Frustration of magnetism in Rb_4O_6 was theoretically analysed in [25]. Within the LSDA, Rb_4O_6 is a half-metal.

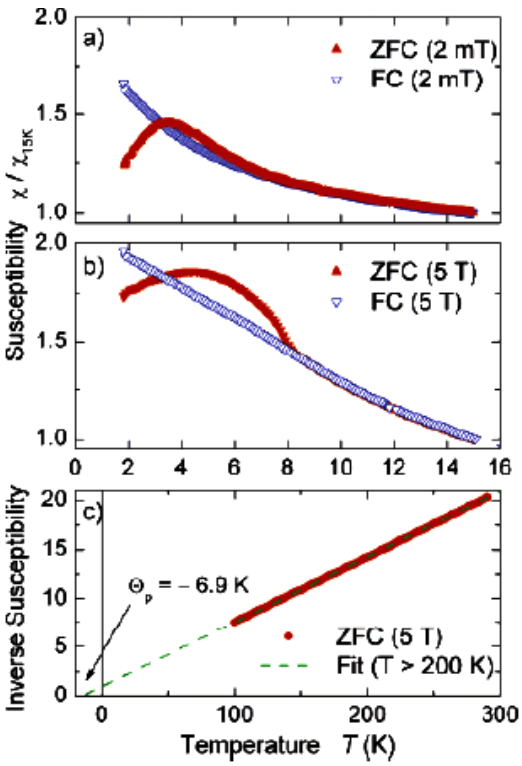

Figure 3.2. Magnetization data for Rb_4O_6. Reproduced with permission from [22]. Copyright 2007 by the American Chemical Society. The low-temperature behaviour of the magnetic susceptibility is shown in (a) and (b) for induction fields of 2 mT and 5 T, respectively. The high-temperature behaviour of the inverse susceptibility for an expanded temperature scale is shown in (c). All values are normalized to the value of the susceptibility at 15 K. Zero-field-cooled data and field-cooled data are denoted by ZFC and FC, respectively.

Inclusion of correlations between the oxygen 2p electrons within the LDA + U properly renders both the insulating character of Rb_4O_6 and its AFM-type magnetic order. For a typical value of U, ~4 eV, the energy of the FM phase is ~80 meV higher than that of the AFM phase. More importantly, the authors analysed a non-collinear magnetic order with spiral modulations. The dependence of energy on the spiral wavevector $\boldsymbol{k}$ is very flat, see figure 3.3, indicative of a degenerate ground state in which a large number of frustrated non-collinear magnetic configurations have a similar energy. Figure 3.3 also shows the calculated configurations of oxygen dimers.

GGA + U calculations were also performed for RbO_2 in the averaged tetragonal structure [26]. Similar to the case of Rb_4O_6, the LSDA or GGA predict the half-metallic behaviour for this compound. Inclusion of the $+U$ corrections results in a tendency towards the formation of an orbitally polarized insulating state in which the symmetry between π_x^* and π_y^* degenerate molecular orbitals of O_2 dimers is lifted by hybridization and electrostatic interactions.

Magnetism of the recently synthesized m-SrN [27, 28] was analysed within the GGA [29]. There are eight atoms of strontium and eight atoms of nitrogen in the unit cell, see figure 3.4. One half of the N ions (denoted by N_{dim}) form

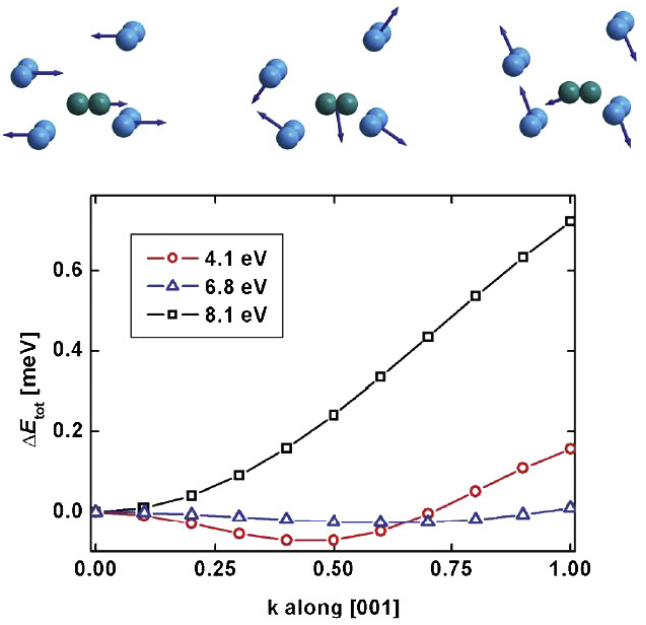

Figure 3.3. The line plot shows the spiral energies of antiferromagnetic Rb_4O_6 as functions of the spiral vector k in units of $2\pi/a$ along the [0, 0, 1] direction for U 4, 1, 6.8 and 8.1 eV. The corresponding magnetic configurations are sketched for $\boldsymbol{k} = 0$, $\boldsymbol{k} = (0, 0, 0.5)$ and $\boldsymbol{k} = (0, 0, 1)$. The energy is given per primitive cell. Reproduced with permission from [25]. Copyright 2009 by the American Physical Society.

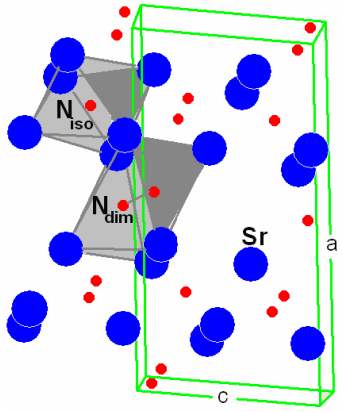

Figure 3.4. Crystal structure of m-SrN. Large blue dots denote Sr and small red ones denote N. N ions forming dimers and isolated N ions are indicated by $N_{\rm dim}$ and $N_{\rm iso}$, respectively.

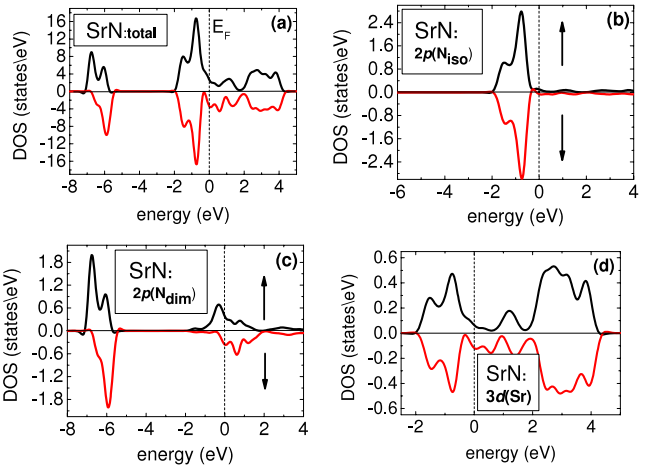

Figure 3.6. Total DOS (a) of FM m-SrN and projections on p states of (b) $N_{\rm iso}$, (c) $N_{\rm dim}$ and on (d) d(Sr). Arrows denote the spin-up and spin-down channels, and vertical dashed lines indicate the Fermi energy. Reproduced with permission from [29]. Copyright 2008 by the American Physical Society.

dimers, while the remaining N ions (denoted by $N_{\rm iso}$) occupy centres of Sr octahedra with a coordination also characteristic for the rock salt phase. As a result of the different coordinations, the two types of N ions, $N_{\rm dim}$ and $N_{\rm iso}$, are in different charge states, and m-SrN is a mixed-valence compound, similarly to Rb_4O_6 and Cs_4O_6. Its formula can be written as $(Sr^{2+})_4(N^{3-})_2(N_2^{2-})$. The calculated heat of formation of m-SrN, $\Delta H_{\rm f} = -0.88$ eV, is lower then that of the rock salt SrN, -0.26 eV, see section 2. This agrees with experiment and shows that the rock salt phase is only metastable.

The different coordinations of the two types of N ions in m-SrN, $N_{\rm dim}$ and $N_{\rm iso}$ result in their different properties reflected in charge and spin densities (see figure 3.5). The contour plot of electron density, figure 3.5(a), shows the molecular bond of N_2, while the spherical shape of charge density around both $N_{\rm iso}$ and Sr indicates the ionic character of bonds between $N_{\rm iso}$ and its Sr neighbours.

This situation is confirmed by the DOS projected on individual atoms shown in figures 3.6(a)–(d). The highest valence bands are mainly formed from nitrogen orbitals. The states at about 1 eV below the Fermi energy originate in p($N_{\rm iso}$) orbitals (figure 3.6(b)) and are occupied by six electrons. This

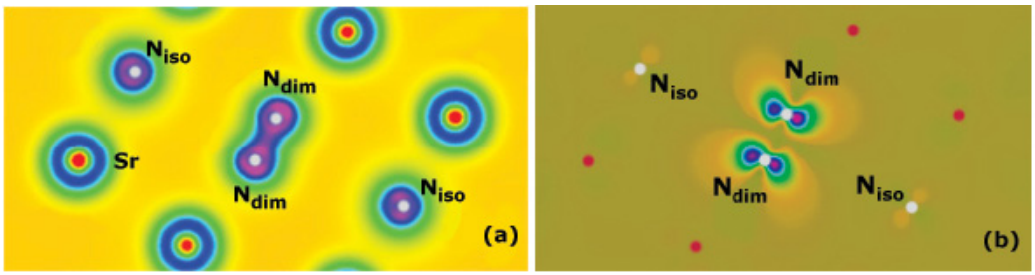

Figure 3.5. Contour plot of (a) the charge density, and (b) the spin density of m-SrN unit cell in the $y = 0$ plane. Sr and N atoms are represented by red and white dots, respectively. N–N dimer is in the middle of the unit cell. Reproduced with permission from [29]. Copyright 2008 by the American Physical Society.

implies that N_{iso} is in the closed-shell three-charge state with vanishing spin, which follows from the symmetry of DOS for up and down spins. The largest and spin-polarized contribution to DOS at the Fermi energy comes from the π states of N_2 dimers, see figure 3.6(c). The contribution of d orbitals of Sr, figure 3.6(d), is only slightly spin-polarized.

The calculated ground state of *m*-SrN is AFM, with a Néel temperature T_N of about 260 K. The FM and the paramagnetic, i.e. non-polarized, phases are higher in energy by 82 and 117 meV/N_2, respectively. We note that the estimated T_N is lower than the room temperature at which *m*-SrN is experimentally found to be paramagnetic [27]. The calculated magnetic moment of N_2 dimers in the two-charge state is 1.6 μ_B. Thus, the electronic configuration is that of the O_2 molecule shown in figure 3.1. In the crystal, the π^* and σ^* orbitals of N_2 are broadened by hybridization with neighbours, and the spin-up and spin-down states overlap, see figure 3.6(d). The Fermi energy falls within the overlap region. This implies that there is a transfer of electrons from spin-up to spin-down states, which reduces the spin moment per N_2 from 2 to 1.6 μ_B. Finally, the magnetic moments of N_{iso} ions vanish because of their closed-shell configuration in the three-charge state. Based on the results of [25, 26] one may expect that inclusion of correlation effects would open the gap, but leave the magnetization less affected.

Localization of the magnetic moments on O_2 or N_2 dimers may suggest that the magnetic order is affected by the dipole–dipole coupling, which is not included in the LDA. Model calculations that assume point-like dipoles located at the N_2 sites in *m*-SrN showed that the dipole–dipole coupling is one order of magnitude weaker than the Heisenberg coupling analysed above [29]. This indicates that the dominant magnetic coupling is mediated by delocalized states from the vicinity of the Fermi level, and that the dipole–dipole interaction provides an additional small contribution to the AFM order. This issue should be examined for Rb_4O_6 and Cs_4O_6, where frustrated magnetism is 'soft', and the contribution of the weak but long-range dipole–dipole coupling can be non-negligible.

4. Magnetism of non-magnetic hosts with non-magnetic defects or dopants

A second class of materials without magnetic ions for which magnetism was considered are crystals with spin moments provided either by dopants or defects. In general, impurities and defects in insulators introduce levels in the bandgap, and electrons that occupy these levels form states with total spin 0 or 1/2. In the latter case, magnetic phases are in principle possible provided that the concentration of defects or dopants is appropriate to enable their coupling. The first part of this section is devoted to vacancies and the second part to dopants.

4.1. High spin states of vacancies

Magnetic properties of vacancies and the possible formation of a magnetic phase were examined in a number of works. One should distinguish two issues in this context. The first one is the electronic structure of an isolated vacancy, and in particular the *local* spin polarization that involves atomic orbitals of the vacancy's neighbours and leads to a high spin configuration. The second problem is the magnetic coupling between vacancies, which may lead to the formation of a *global* magnetic phase in a defected crystal. These issues are related to some extent since, as we show below, the radius of the coupling between vacancies depends on their electronic structure.

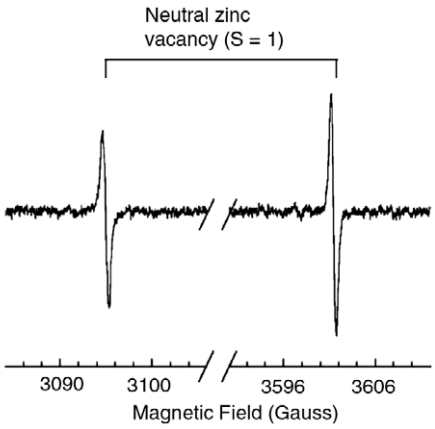

Figure 4.1. EPR spectrum of the neutral zinc vacancy V_{Zn} in an electron-irradiated ZnO crystal. Data taken at 30 K after a brief exposure to 325 nm laser light. Reproduced with permission from [31]. Copyright 2008 by the American Institute of Physics.

In cubic crystals, defect-induced states can be singly, doubly or triply orbitally degenerate. Thus, the highest possible spin state is $S = 3/2$, which occurs when the defect-induced level is a half-occupied triplet. Typically, however, defects in semiconductors assume low spin configurations with total spin 0 or 1/2, depending on the defect's charge state, i.e. on the number of electrons that occupy the defect state. Here, the noticeable exceptions are states of cation vacancies in several semiconductors, which exhibit high spin states.

The first experimental observations of high spin states of cation vacancies were reported for II–VI oxides about four decades ago. More specifically, the zinc vacancy V_{Zn} in the $S = 1$ high spin state was identified in electron-irradiated ZnO [30], where the observed signals corresponding to $S = 1$ and 1/2 were proposed to originate in the neutral and the negative charge state of V_{Zn}, respectively. Recently, a more detailed study of V_{Zn} in ZnO was reported in [31], see figure 4.1. Two non-equivalent configurations of the negatively charged V_{Zn} are seen. In wurtzite ZnO, a trigonal Jahn–Teller distortion occurs for V_{Zn}, with the trapped hole localized primarily on one of the four nearest oxygen neighbours. The axial centres (i.e. with O neighbour along the *c* axis) and nonaxial ones (with three O neighbours in the basal plane) are inequivalent, the nonaxial ones being energetically preferred and significantly stronger. Another $S = 1$ spin state observed in electron-irradiated ZnO was identified as arising from an exchange-coupled state made up from a separated shallow donor and a zinc-vacancy-related centre, most probably a Frenkel pair [32]. The high spin $S = 1$ state of neutral Mg vacancies was then observed in MgO [33, 34]. A neutral gallium vacancy, V_{Ga}, in the irradiated GaP was studied

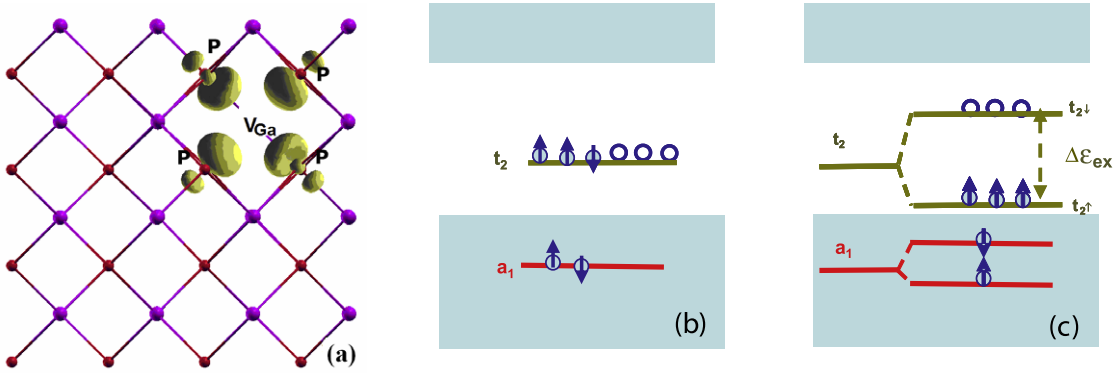

Figure 4.2. Typical electronic structure of a cation vacancy in zb-III–V semiconductors. Four sp^3 orbitals of four neighbouring anions in GaP (a) introduce a singlet a_1 and a triplet t_2 (b), which are split into spin-up and spin-down states in the case of a non-vanishing spin polarization (c). Filled and empty circles in (b) and (c) indicate occupied and empty states, respectively.

in [35]. Analysis of electron paramagnetic resonance (EPR) spectra, performed under uniaxial strain, was able to non-ambiguously determine that V_{Ga} is in the high spin $S = 3/2$ state. Finally, the negatively charged silicon vacancy has a high spin configuration with $S = 3/2$ in both zinc blende and 4H polytypes of SiC [36, 37].

Stability of a high spin configuration of a vacancy was theoretically first examined for a silicon vacancy in SiC. Detailed studies [38–40] showed that for the neutral, singly and doubly negative charge states q of V_{Si} a strong exchange coupling, which prefers a parallel electron spin configuration, overcomes the Jahn–Teller energy. For other charge states the ground state of V_{Si} has a low spin configuration. According to [38], in zb–SiC the spin polarization energy is 0.58 eV for $q = -1$, and about 0.4 eV for $q = 0$ and -2; for these three charge states the high spin of V_{Si} is stable also in the wurtzite 2H-SiC. Similar results were obtained in [40]. A high spin state is also predicted for a silicon vacancy in SiGe [41], but the polarization energy is low, about 20 meV.

Subsequent first-principles calculations predicted the stability of the high spin state of neutral cation vacancies in CaO [42, 43] and HfO_2 [44, 45] in which symmetry-lowering relaxations have a considerable impact on electron density [43], III-N nitrides [46–49], MgO [49, 50], ZnO [11, 47] and in ZnA (A = O, S, Se, Te) II–VI compounds [51]. In the latter paper it was found that the high spin state is stable only in ZnO; this result was attributed to the high ionicity of ZnO. In [52] the important role of electronic correlations is demonstrated, but the inclusion of spin–orbit coupling [9], especially for heavy Se and Te, can affect the final conclusions. Model unrestricted Hartree–Fock calculations were used to study the formation of a magnetic phase in oxide compounds [53]. Analysis of the results presented in the following demonstrates that the high spin configuration of vacancies and spin polarization of bulk crystals discussed above are of the same physical origin, which is the strong spin polarization of C, N and O atoms.

Formation of a cation vacancy, V_{cation}, in the zinc blende or wurtzite structure results in formation of four dangling bonds of the four anion neighbours of the vacancy, figure 4.2. They combine into a non-degenerate level a_1 and a triply degenerate level t_2 that is higher in energy. Energies of a_1 and t_2 relative to the top of the valence band (VBT) depend on the crystal. Typically, in the case of a neutral V_{cation}, a_1 is fully occupied and is a resonance with valence bands, while t_2 is in the bandgap and is occupied by two, three or four electrons in group IV, III–V or II–VI compounds, respectively.

In the low spin configuration, total spin is $S = 0$ or $1/2$, depending on the number of electrons occupying the triplet. The low and high spin states of neutral V_{Ga} in GaP are shown in figures 4.2(b) and (c), respectively. In the case of a non-vanishing spin polarization, the exchange coupling splits t_2 into spin-up ($t_{2\uparrow}$) and spin-down ($t_{2\downarrow}$) states by $\Delta\varepsilon_{ex} = t_{2\downarrow} - t_{2\uparrow}$. In this case, a_1 is also split into spin-up ($a_{2\uparrow}$) and spin-down ($a_{2\downarrow}$) states. When $t_{2\uparrow}$ is a resonance, $\Delta\varepsilon_{ex}$ can be defined as $2(t_{2\downarrow} - t_2)$ because the energy of $t_{2\uparrow}$ cannot be accurately assessed. Stability of various spin configurations is given by spin polarization energy ΔE^{H-L}, defined as the difference in total energy of the high spin and spin-non-polarized states. The high spin state is stable if $\Delta E^{H-L} < 0$ and $\Delta\varepsilon_{ex} \neq 0$.

The calculated electronic structure of a neutral V_{Ga} in the series GaAs, GaP, GaN and AlN in the zinc blende phase is shown in figure 4.3 [47]. The results obtained for w-GaN and w-AlN are similar in terms of spin polarization energies and position of vacancy levels, as expected. V_{Ga} in GaAs introduces the triplet t_2 at 0.4 eV above the top of the valence band. The high spin state is unstable since the initially imposed high spin configuration decays into the low spin state with the total spin $S = 1/2$ and $\Delta\varepsilon_{ex}$ vanishes. In GaAs, GaP and GaN the vacancy-induced singlet a_1 is a resonance in the valence band. In the case of V_{Ga} in GaP, t_2 is 0.3 eV above VBT. The high spin state is stable with $\Delta E^{H-L} = -0.06$ eV, t_2 is split into spin-up $t_{2\uparrow}$ (occupied with three electrons) and (empty) $t_{2\downarrow}$ spin-down states by $\Delta\varepsilon_{ex} = 0.19$ eV, and the total magnetic moment $\mu_{tot} = 3\ \mu_B$ in agreement with experiment [35]. The t_2 state of V_{Ga} in GaN is 0.22 eV above VBT. The high spin state with $\Delta E^{H-L} = -0.69$ eV is, by an order of magnitude, more stable than in GaP. The spin splitting of t_2 is large, $\Delta\varepsilon_{ex} = 0.78$ eV. Consequently, and in contrast to GaP, $t_{2\uparrow}$ is a resonance degenerate with the valence bands, while $t_{2\downarrow}$ is 0.6 eV above VBT and is empty. The resonant character of $t_{2\uparrow}$ is important, because it affects the spatial extension

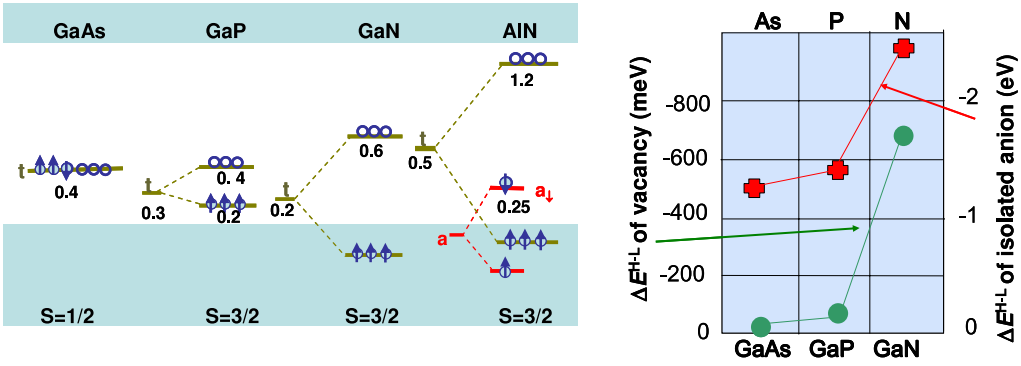

(a) **(b)**

Figure 4.3. (a) Electronic structures of neutral V_{Ga} in zb–GaAs, GaP, GaN and AlN. t denote the t_2 state. The numbers give energies relative to VBT in eV. Conduction band is shown only schematically, and does not reflect the actual value of the bandgap. Spins of electrons are indicated by arrows, empty spheres indicate unoccupied states. (b) The energy of spin polarization of neutral V_{Ga} in zb–GaAs, GaP and GaN and energy of spin polarization of isolated As, P and N. Reproduced with permission from [47].

of the wavefunction, and thus the vacancy–vacancy magnetic coupling, see below. Finally, t_2 of V_{Al} in AlN is 0.54 eV above VBT, the high spin state is stable with $\Delta E^{H-L} = -0.93$ eV and $\Delta\varepsilon_{ex} = 1.3$ eV, which shows that spin polarization in AlN is stronger than in GaN. $t_{2\uparrow}$ is a resonance occupied by three electrons with parallel spins. Interestingly, non-polarized calculations give the a_1 singlet situated in the valence band close to VBT; inclusion of spin polarization leads to a strong a_1 splitting as well, and $a_{1\downarrow}$ occupied with one electron is in the bandgap at 0.25 eV above VBT. Note that in this case the $a_{1\downarrow}$–$t_{2\downarrow}$ crystal field splitting is 0.95 eV, and is well defined.

The states of V_{Zn} in w-ZnO are built from p(O) orbitals and are occupied with six electrons. The vacancy introduces a triplet t_2 in the bandgap close to VBT, split by the crystal field with a small splitting energy of ∼0.1 eV. The triplet is spin-split by the exchange interaction: however, $t_{2\uparrow}$ is not a resonance because $\Delta\varepsilon_{ex} = 0.11$ eV, which is smaller than in III–V nitrides. V_{Zn} is stable in the $S = 1$ high spin state with $\Delta E^{H-L} = -0.04$ eV [11, 47], in agreement with experiment [30, 31].

Figure 4.4 compares spin density of vacancies in SiC and GaN. In the case of both V_{Si} in SiC [47] and V_{Ga} in GaP (figure 4.2), the main contribution is given by the orbitals of the vacancy's neighbours and is strongly localized because both $t_{2\downarrow}$ and $t_{2\uparrow}$ are in the bandgap. In contrast, in III–V nitrides the triplet $t_{2\uparrow}$ is a resonance degenerate with valence bands. Consequently, $t_{2\uparrow}$ hybridizes with the states from the upper part of the valence band (which are mainly formed from the p(N) orbitals) and the spin polarization contains both a localized contribution of sp^3 orbitals of the vacancy neighbours and a fairly long-ranged tail, see figure 4.4(b). However, the localized part is dominant, which explains why the spin polarization persists even in the case when t_2 is a resonance. The long-range tail of spin polarization affects the magnetic coupling between vacancies and thus their possible collective magnetic order.

We also briefly mention the interplay between charge and spin states. For example, a neutral V_{Ga} in GaP is stable in the high spin $S = 3/2$ state, while for both $q = 1+$ and $1-$ there is $\Delta E^{H-L} = 0$ [47]. Thus, charged vacancies in GaP have the low spin $S = 0$ configurations, and indeed spin states other than 3/2 were not observed. In contrast, the spin polarization of V_{Ga} in GaN and AlN survives also for $q = -1$ because the atomic spin polarization of N is stronger than that of P [47], see figure 4.3(b).

Figure 4.5(a) summarizes the calculated values of ΔE^{H-L} and $\Delta\varepsilon_{ex}$ for GaP, GaN, AlN and ZnO [47]. One can see that ΔE^{H-L} increases with the increasing $\Delta\varepsilon_{ex}$. This correlation takes place because the energy gain ΔE^{H-L} induced by the formation of the high spin state is partially provided by the energy gain of the electronic contribution to the total energy. This mechanism is illustrated in figure 4.5(b). In particular, this picture qualitatively explains why the calculated spin polarization energy ΔE^{H-L} is the highest when the t_2 state is occupied with three electrons, while for other occupations the high spin state is less stable, or vanishes like in GaP. This argument also accounts for the lower energy of spin polarization of a neutral vacancy in ZnO (where t_2 is occupied with four electrons) than that of a neutral vacancy in III–V nitrides (where t_2 is occupied with three electrons). However, if this mechanism would account for the entire energy of spin polarization, the relation $\Delta E^{H-L} = (3/2)\Delta\varepsilon_{ex}$ should be obeyed for neutral V_{cation} in III–V compounds. This is not the case: from the obtained results it follows that this factor accounts for about one-half of ΔE^{H-L}, which indicates that other factors play an important role. An empirical model, such as that developed in [51], could provide a deeper insight into the problem.

4.2. Magnetism induced by vacancies

Collective magnetism induced by vacancies was first considered for V_{Ca} in CaO in [42], where it was suggested that sufficiently high concentrations of vacancies may lead to an FM phase. (Note that in this context formation of a high spin state of V_{Ca} is advantageous, because the magnetic coupling is in general proportional to the spin squared.) This issue was next examined in [43], where it was shown that

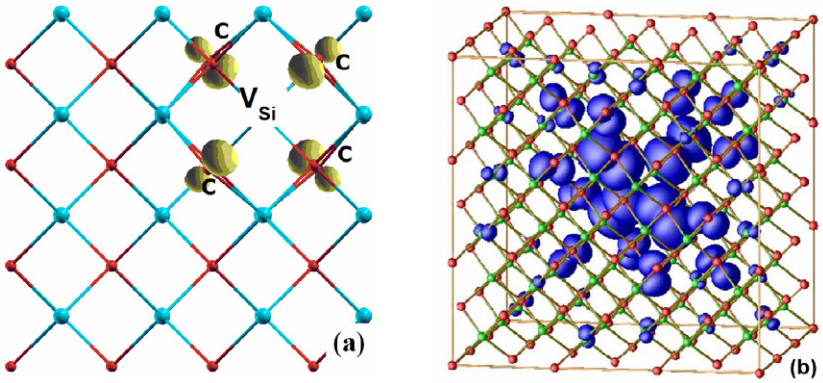

Figure 4.4. Spin density of (a) V_{Si} in zb–SiC for 64-atom unit cells [47], and (b) V_{Ga} in zb–GaN for a 216-atom unit cell. Reproduced with permission from [48]. Copyright 2008 by the American Physical Society.

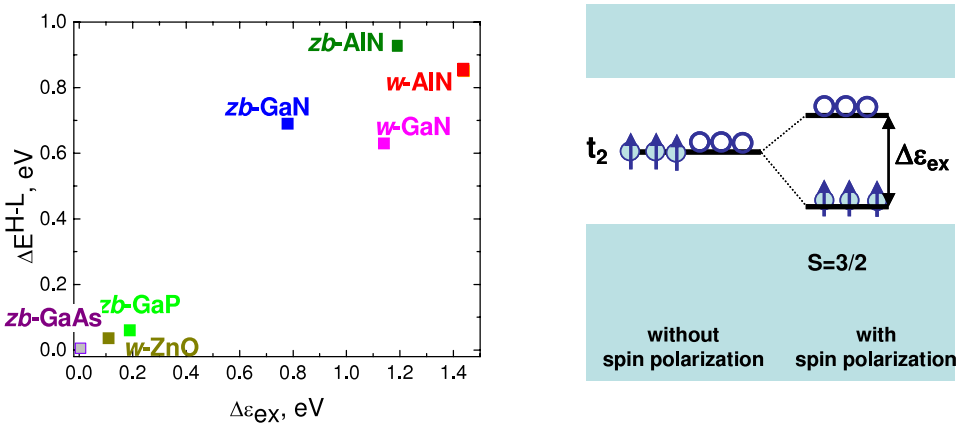

Figure 4.5. Left panel: the dependence of the energy of spin polarization of vacancies on exchange splitting of t_2 levels for neutral vacancies. Right panel: the scheme explaining the energy gain from the electronic contribution of the triplet state to the spin polarization of the vacancy. Reproduced with permission from [47].

the ferromagnetic interaction between two vacancies in CaO extends only to four neighbours or less. To achieve magnetic percolation on an fcc lattice with such an interaction range one needs a minimum of 4.9% vacancies, or a concentration about 2×10^{21} cm^{-3}. On the other hand, total energy calculations show that, due to the high vacancy formation energy, even under the most favourable growth conditions one cannot obtain more than about 10^{18} cm^{-3} vacancies at equilibrium. This demonstrates that a (nonequilibrium) vacancy concentration should be three orders of magnitude higher than the equilibrium value to achieve magnetism in such systems. However, magnetic coupling in semiconductors can be modified by doping which changes the charge state of magnetic centres and/or introduces free carriers that may mediate magnetic coupling. In [11] it was shown that high concentrations of holes in ZnO quantum wells enhance magnetic coupling and result in FM. This method of achieving FM may be more efficient than the increase of the concentration of vacancies, since with the decreasing separation between vacancies their magnetic moment decreases and can eventually vanish [11].

The vacancy–vacancy coupling in GaN and BN is different: the results of [48] demonstrate that the coupling between neutral V_{Ga} is AFM. However, it changes sign to FM for V_{Ga} for the negative charge states, i.e. upon n-type doping. In the latter case, the defect concentration of 0.9% may result in an FM phase, which follows from the relatively long-range character of the interaction discussed above, see figure 4.4. However, since the formation energy of V_{Ga} is very large [54], such high concentrations of vacancies are orders of magnitude above the equilibrium value.

Schematics of the electronic structure of an acceptor level induced by a vacancy or impurity, and coupling between a pair of defects, are shown in figure 4.6. The triplet state occupied with three electrons is split into spin-up and spin-down states by the exchange interaction (a). Coupling between two defects (b) splits all states into bonding and antibonding combinations. In the case of a neutral V_{Ga} in GaN, the spin-up subband is fully occupied, the energy gain vanishes and the magnetic interaction between vacancies is superexchange and AFM [48]. In contrast, in the case of a neutral V_{Zn} in ZnO with one electron on the spin-down state the energy gain favours FM coupling, figure 4.6(c).

4.3. Impurity-induced magnetism: role of electron correlations

Experimental observation of FM in a doped semiconductor was reported in [55], where the authors analysed ZnO containing

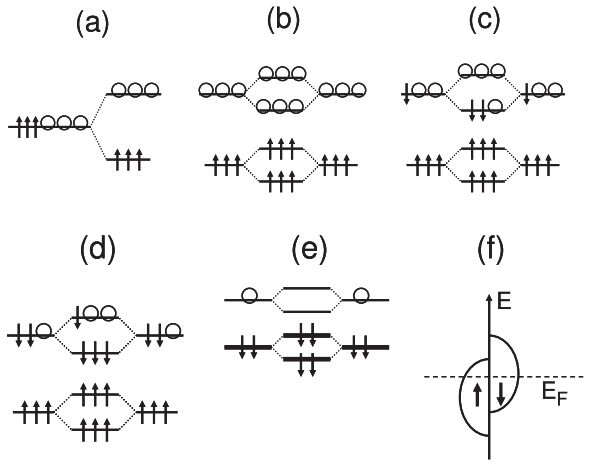

Figure 4.6. Scheme of the electronic structure of a triplet state induced by a defect (vacancy or impurity), and the mechanism of the coupling between a pair of defects with various occupations. Arrows and dots represent electrons and holes, respectively. See the text.

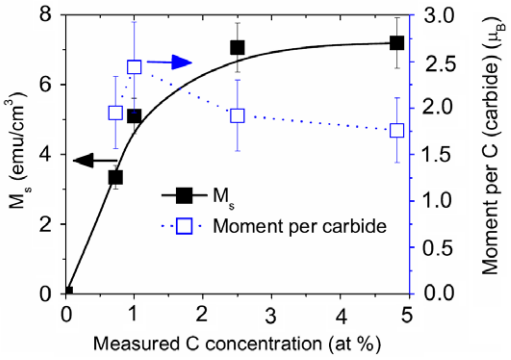

Figure 4.7. The room-temperature saturation magnetization M_s and the magnetic moment per carbon in the carbide state as a function of the measured carbon concentration of the C-doped ZnO. Reproduced with permission from [55]. Copyright 2007 by the American Physical Society.

1–5% of C and found impressive Curie temperatures exceeding 400 K, which is about three times higher than T_C of the most studied dilute magnetic semiconductor (GaMn)As. The measured magnetic moment is about 2 μ_B per C atom, figure 4.7, in agreement with the calculated value. This result is important, since it demonstrates that magnetism does not stem from trace concentrations of magnetic contaminants in the samples. Theoretical results indicated that FM can be due to the spin polarization of electrons in the C-induced and partially filled impurity band, and that the presence of additional holes can enhance FM [55]. Subsequently, room-temperature FM was observed in thin ZnO films [56] and ZnO nanoneedles [57] containing 2–8% of carbon. Consistent with [55], the magnetic moment is about 2 μ_B per C atom in both works, and the anomalous Hall effect is seen. A spin-glass type behaviour is observed up to 50 K, but FM is dominant [56, 57]. Interestingly, temperature dependences of the magnetic and transport properties seem to be only weakly correlated: magnetization exhibits a smooth behaviour in the temperature range 50–350 K, while conductivity increases by one order of magnitude in the temperature window 230–280 K in which it changes its character from variable-range hopping to metallic-like conductivity. Next, C substituting for O is a double acceptor, but ZnO:C samples investigated in [55] are weakly n-type, which may indicate the presence of compensating defects and/or of hydrogen typical for ZnO, and which somewhat questions the partial occupation of the C-induced band that is a prerequisite for the FM phase, see below. In contrast, ZnO specimens of [56, 57] are p-type. Without questioning the importance of the discoveries of [55–57] one may observe that, in order to understand transport and magnetic properties, further studies are needed, including the atomic-scale morphology. In particular, control of the coupling between spin and charge degrees of freedom could lead to functionalization of ZnO:C in spintronics applications. From this point of view, AlN and GaN doped with C that preferentially substitutes N [58] may be superior to ZnO:N since GaN technology is better controlled.

As suggested in [55], co-doping with nitrogen should enhance the magnetism of ZnO:C. Magnetism of ZnO co-doped with C and N was observed in [59], but the magnetic moment per carbon atom was small, 0.05 μ_B, and it decreased to 0.004 μ_B in samples co-doped with N. Moreover, the samples were n-type, which implies that N and C acceptor states are fully occupied with electrons, and this is not consistent with the idea of magnetism induced in a partially occupied acceptor band. Room-temperature FM was also reported for N-doped ZnO [60], but again the samples were n-type. Finally, experimental results showed that a substitution of nitrogen for oxygen in non-magnetic SrO oxide leads to holes in p(N) states (as expected for acceptors) that form local magnetic moments [61]. The nitrogen 1s core-level x-ray photoemission spectroscopy confirmed spin polarization of nitrogen, but magnetic properties of Sr(O, N) were not assessed.

Theoretical studies of impurity-induced magnetism comprise diamond [62], II–VI oxides (ZnO, MgO, CaO and SrO), GaN doped with C and N, and ZrO_2 doped with group I^A and II^A elements [63]. First-principles calculations of [64] predicted formation of the C-induced impurity band in MgO, CaO and SrO that is spin-polarized, which leads to FM for concentrations higher than about 1%. Results are discussed within the Stoner model, and the authors point out the impact of the width of the impurity band (determined both by the impurity concentration and the lattice constant of the host) on the magnetic coupling. The calculations were also performed for diamond co-doped with interstitial hydrogen (naturally present in diamond) and B or P [62]. For the concentration of 1% of H, a fully spin-polarized band forms, but the magnetic ground state is spin-glass-like, without a preferred spin orientation. When samples are co-doped with 0.5% of B acceptor (P donor), a spin-up (spin-down) subband is half-filled and spin polarization is stable. Ferromagnetism in ZnO was predicted by first-principles calculations for nitrogen which is a single acceptor [61, 65, 66], and the double acceptor C [11].

Mechanism of the FM coupling is schematically shown in figures 4.6(c) and (d). In the case of C in ZnO with one

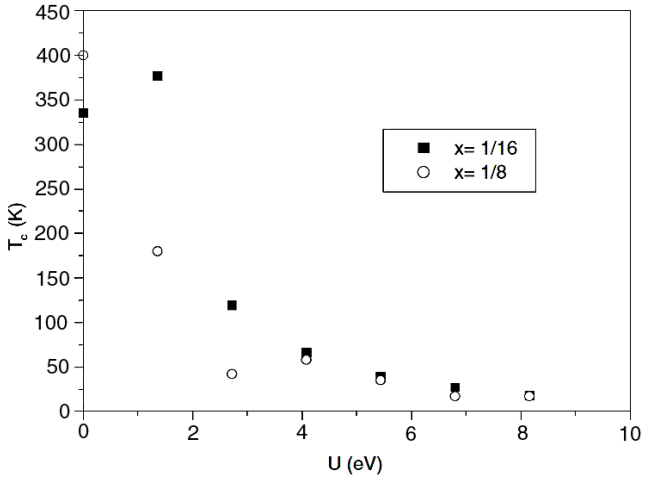

Figure 4.8. Strength of the magnetic coupling in MgO:N obtained from LSDA + U calculations (including spin–orbit coupling) with various values of U calculated in terms of the Curie temperature. Reproduced with permission from [67]. Copyright 2008 by the American Physical Society.

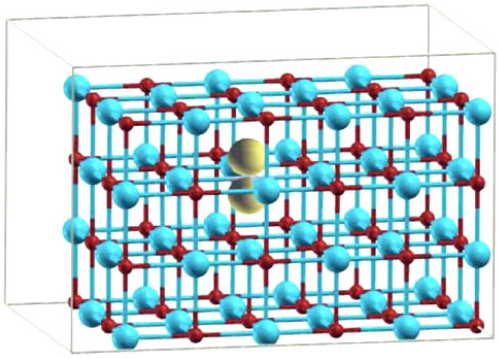

Figure 4.9. Magnetization isosurfaces calculated with SIC for N_O in MgO. Note that the $S = 1/2$ hole is completely localized along the p_z orbital and is not evenly distributed along all the bonds. The large spheres are Mg and the smaller spheres are O ions. N is not displayed for clarity. Reproduced with permission from [49]. Copyright 2008 by the American Physical Society.

electron in the spin-down state, the FM configuration between two C atoms is energetically favoured. For N in ZnO, two electrons occupy the spin-down triplet, and FM coupling is still favoured. Finally, with the increasing concentration of impurities the levels are broadened into bands, and spin-up and spin-down bands can overlap, figure 4.6(f). This reduces the magnetic moments and the degree of spin polarization also in the case of vacancies and molecular magnets.

Recent works devoted to alkaline earth monoxides and GaN [49, 61, 67] raise a very important question of the role of electron correlations. The local density approximation is known to underestimate Coulomb repulsion and overestimate the delocalization of the charge density. This can lead to a spurious metallicity of insulating systems and an overestimation of magnetic coupling. In [67] the results of LSDA and LSDA + U calculations were compared for N acceptors in MgO and other II–VI compounds. Strong FM coupling is obtained in the $U = 0$ itinerant electron limit, but it decreases strongly in the localized limit, in which the Coulomb repulsion within the p(N) shell is much greater than the N-induced impurity bandwidth. The main effect of $+U$ correction consists in breaking the symmetry between three N–Mg bonds due to the Jahn–Teller effect. In the final configuration four of the six Mg–N bonds are filled, while the two remaining are empty, longer by about 3%, and 2 eV higher in energy due to the Jahn–Teller crystal field splitting. Calculations for SrO:N provide the same picture [61]. The splitting increases with U and a metal–insulator transition takes place, which limits magnetic coupling. The strong Jahn–Teller effect found within LDA + U is presented in figure 4.6(e), it splits the spin-down triplet into a doublet and a singlet. For clarity, spin-up states are not shown. In this case, the FM configuration is no longer favoured and a superexchange interaction may be dominant. The dependence of the coupling on U is illustrated in figure 4.8 for MgO:N. The Curie temperature was obtained from the mean-field approximation using the calculated coupling constants. Typical values of U are ∼5 eV, for which T_C decreases by an order of magnitude, see figure 4.8.

A similar conclusion follows from the study based on the self-interaction correction (SIC) scheme of B, C and N substituting oxygen (i.e. triple, double and single acceptor, respectively) in rs–MgO [49]. LSDA calculations predict the formation of a spin-polarized phase and a fully symmetric relaxation around N. Inclusion of SIC leads to two N–O bonds being longer than the remaining ones, which is accompanied by a splitting of the N-induced triplet by about 3 eV, and causes the system to be insulating. Magnetization isosurfaces are shown in figure 4.9. Consequently, the magnetic coupling changes from a Zener mechanism to a weaker superexchange.

On the other hand, recent work on MgO:N [66] presents sound arguments in favour of a less important role of correlations than that assumed in [49, 61, 67]. More specifically, analysis shows that the wavefunction of N impurities in MgO extends over a few ångströms, i.e. twelve oxygen neighbours of N, which is an order of magnitude more than the radius of the d orbitals of transition metals. Note that an even higher delocalization characterizes the wavefunction of vacancies in GaN, figure 4.4. This implies that electron correlation effects may indeed be less critical than in strongly correlated systems. Similarly, even in the case of a transition metal Cu impurity in ZnO the best agreement with experiment is obtained for $U = 1$ eV [68]. Such a low value of U has only a minor impact on the results obtained within the GGA or LDA. Clearly, the role of electron correlations is important for understanding p-based magnetism, but this question is open at present.

5. Graphite and nanographite

The topic of molecular magnets was reviewed in [69] and will not be discussed here. It should be pointed out, however, that the first material which showed well-defined bulk ferromagnetism without transition metal ions is p-NPNN

($C_{13}H_{16}N_3O_4$), even though the Curie temperature T_C was low, 0.6 K [70]. The field is quite active and several recent works reported ferromagnetism in C_{60}-based polymers [71–73]. In particular, azafulleren $C_{59}N$ that is formed by replacing a single carbon atom of the C_{60} by a nitrogen atom [74, 75] and the N–C_{60} molecule [76, 77] have magnetic moments. Ferromagnetism in these systems is weak, since typical Curie temperatures do not exceed 15 K, which is not promising for applications. On the other hand, carbon nanoparticles produced by a pulsed arc submerged in ethanol exhibit FM with T_C much higher than 300 K [78].

Ferromagnetism was observed in several organic materials, mainly in various forms of graphite and graphene. Low-temperature disordered magnetism in activated carbon fibres was reported in [79] and was ascribed to random strengths of AFM interactions between nanographites constituting the system, and which are mediated by carriers. Higher Curie temperatures (up to 90 K) characterize carbon nanofoam obtained by high-repetition-rate, high-power laser ablation of glassy carbon [80]. This discovery was unexpected since bulk graphite is diamagnetic. In particular, experiments demonstrated the presence of ferromagnetic-like features in pyrolytic graphite [81]. Robust magnetic order at room temperature was observed in graphite [82] as well as in thin carbon films after proton irradiation [83]. The results obtained in the latter work are shown in figure 5.1. Carbon films of about 200 nm thickness were grown by pulsed-laser deposition. The samples were then irradiated by 2.25 MeV protons using a focused proton beam to produce an array of magnetic spots with different fluences. One can identify the beam impact area in the middle of the spot shown in figure 5.1. The middle area does not show any contrast in the magnetic force microscopy (MFM) images, while the ring-shaped area surrounding the point of impact does, altogether MFM suggests that magnetic order is induced by the proton irradiation in the area surrounding the beam impact area for the fluence used. Irradiation-induced ferromagnetism at room temperature was also observed after implantation of C and N in carbon nanosized particles [84]. The saturation magnetization is higher for N-implanted samples at higher doses, which indicates that not only the generated defects but also the chemical nature of the implanted species may play a role in the formation of the magnetic phase. These experiments undoubtedly demonstrate that FM does not originate in the presence of magnetic contaminations such as Fe ions, and they relate magnetism to defects in graphite. However, it is necessary to stress that the origin of the magnetic properties of organic materials are still under debate, and can depend upon sample preparation.

From the theoretical side, magnetic properties of graphite were proposed to originate in the presence of two point defects, namely vacancies and hydrogen atoms [85–87]. Both defects are very likely to form during proton irradiation of graphite. In this case, magnetization increases with the increasing irradiation dose [82], which can be connected with the increasing concentration of defects.

In [85], properties of isolated vacancies and vacancy–hydrogen complexes were studied. It was shown that both

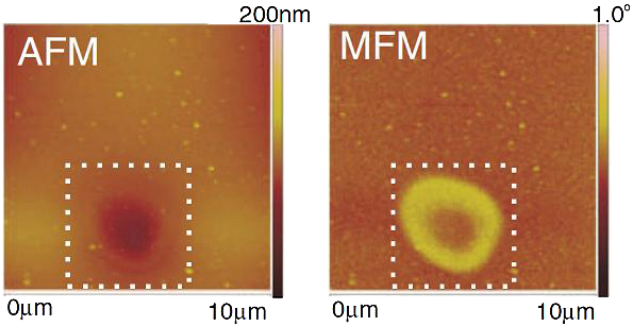

Figure 5.1. Atomic force microscopy (AFM) and MFM images of a spot irradiated with a 2.25 MeV proton beam and a fluence of 50 nC μm^{-2}. The field of view is 10 μm. The AFM image reveals the beam impact area. A line scan through its centre reveals a deepening of about 70 nm depth in 5 μm distance. The MFM image suggests a magnetic 'ring' around the impact area. The measurements were done at ambient conditions using a low moment tip and without applying any magnetic field. Reproduced with permission from [83]. Copyright 2007 by the American Physical Society.

defects possess localized spin moments, and thus may lead to magnetism. A vacancy undergoes the Jahn–Teller distortion upon relaxation [85, 88], where two of the nearest atoms to the vacancy site form a weak covalent bond, resulting in a pentagon-like structure, with the final atom displacing by 0.18 Å out of the surface plane [85]. The ground state of the vacancy has spin $\approx$1 μ_B, and spin density is localized on the broken bond of carbon. Furthermore, adsorption of H on one of the dangling bonds of a vacancy gives rise to a magnetic moment twice as high as that of a bare vacancy [85]. It was also shown that hydrogen strongly adsorbs at vacancies maintaining the magnetic moment of the defect, and that for small irradiation doses vacancy–hydrogen complexes should give rise to a macroscopic magnetic signal, which agrees very well with the experimental values. At the same time, absorption of H should suppress recombination of vacancy-interstitial Frenkel pairs. Thus, these results stress the importance of hydrogen for the development of the magnetic state and offer a possible explanation for the results of experiments on graphite irradiation with H and He ions: hydrogen irradiation should result in a much stronger magnetic signal. On the other hand, experimental data indicate that magnetization in highly oriented pyrolytic graphite (HOPG) should be due to hydrogen present in samples prior to irradiation [83].

Theoretical calculations show that magnetic coupling between vacancies is relatively short range, since vacancies distant by more than 7 Å are not coupled [87]. This implies a high percolation limit exceeding 4% for the formation of a magnetic phase based on the vacancy–vacancy coupling. Next, while the total magnetization decreases with the increasing density of vacancies for both diamond and graphite, magnetization decreases more rapidly for graphitic structures, thus making the cooperative magnetic phase more difficult to form. Finally, the presence of nitrogen impurity in the vicinity of a vacancy was shown to produce larger macroscopic magnetic signals compared to an isolated vacancy, which may partially explain the data of [84].

The second source of magnetization in graphite is planar defects. Grain boundaries are one of the most commonly occurring extended defects in HOPG because of its polycrystalline character. Mombru *et al* [89] have observed multilevel FM behaviour of graphite at room temperature. By magnetic force microscopy the authors verified that its magnetic properties are related to the topographic defects introduced in the pristine material. The recent experimental study [90] was performed using MFM and bulk magnetization measurements. Correlation between topography, magnetic and electrostatic signals on the graphite surface show the presence of line defects and a clear indication of ferromagnetic order at the defect sites at room temperature. More details on the formation of periodic structures along grain boundaries are reported in [91]. Detailed STM and AFM pictures allow possible microscopic configurations at the boundaries to be proposed.

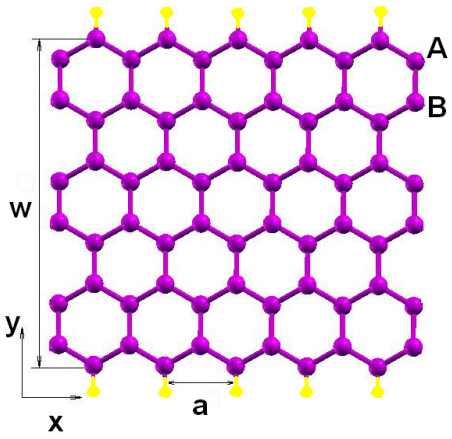

Figure 6.1. A carbon nanoribbon with six zigzag chains. The system is periodic along the x direction. The two sublattices are labelled A and B, respectively. The edges along the y direction have the armchair termination. Magenta and yellow dots indicate, respectively, C and H atoms.

6. Graphene ribbons

Nanoscale carbon materials, such as carbon nanotubes and fullerenes, have attracted attention in the past two decades both because of the fundamental scientific interest in this novel family [92] and because of their particular electronic properties that are expected to find applications in future nanoelectronics [93]. In particular, graphene is the subject of extensive experimental and theoretical research. The field is progressing rapidly and any review is almost dated when appearing in print. In this situation we only summarize the main results pertinent to magnetism based on p orbitals. Several excellent reviews are available [94].

The electronic structure of bulk graphite and of 'a single hexagonal layer' (i.e. graphene) within a simple tight binding model based on s and p orbitals of carbon was first described in [95]. Recently, a comprehensive discussion of the band structure of pristine graphene was provided in reviews [96, 97]. Graphene forms a biparticle lattice, i.e. its unit cell contains two carbon atoms which give rise to two sublattices. In the simplest approach, bonds and bands formed from the sp^2 carbon orbitals are assumed to be filled and inert, while wavefunctions of the conduction holes and electrons are formed from the p_z carbon orbitals perpendicular to the plane of graphene. The valence and the conduction band are degenerate at two non-equivalent points in the Brillouin zone, thus graphene is a zero-gap semiconductor. In the vicinity of these points, both the filled valence and the empty conduction bands have a linear dispersion to a good approximation.

Finite-sized pieces of graphene with nanometre dimensions, the so-called nanoribbons, can be obtained. Theoretical results show an unexpectedly rich behaviour of their electronic structure, which differs from that of the 'bulk' graphene, and is largely determined by the presence and the type of edges. There are two simple generic terminations of a nanoribbon, namely the zigzag and the armchair edges, which are shown in figure 6.1. The corresponding nanoribbons are usually referred to as zigzag (ZN) or armchair (AN) ones.

The question of the relative stability of various terminations of graphene ribbons awaits a definite answer. Theoretically, the stability of both armchair and zigzag edges was examined in [99]. The results suggest that the zigzag edge is unstable with respect to reconstruction consisting in the formation of a pentagon and a heptagon from two adjacent hexagons. Such a reconstructed zigzag edge has the lowest formation energy, but the energy of an armchair edge is very close. Experimentally, the reconstructed zigzag edge was not identified [100–105]. The measurements of [101] indicate that armchair edges form more easily, and thus are more stable than zigzag edges. On the other hand, recent impressive experiments using transmission electron microscopy [103] demonstrate a higher stability of the zigzag edge.

According to the established convention, the nanoribbons with armchair edges on both sides are classified by the number (N_a) of dimer lines contained in the ribbon width. Similarly, the ribbons terminated by zigzag edges on both sides are classified by the number of zigzag chains (N_z). In general, the finite size of ribbons is expected to open the width-dependent bandgap due to quantum confinement effects. The actual situation is more complex. ARs form three families that are labelled by mod $(N_a, 3) = 0$, 1 or 2, respectively. Simple tight binding calculations [106, 107][4] showed that the members of the '2' family (i.e. ribbons with $N_a = 3n + 2$, where n is an integer) are always metallic, while the ARs from the '0' and '1' families are insulating. The subsequent first-principles calculations [108] showed that all three families are insulators, with the gap decreasing with increasing width, as expected, but the size dependence of the bandgap is different for the '0', '1' and '2' families. Importantly, all ARs are non-magnetic and thus are not within the scope of the present review.

In contrast, zigzag nanoribbons are of interest for us because their edges induce localized edge states which are spin-polarized. The initial model tight-binding calculations neglected spin polarization and predicted a vanishing bandgap

[4] Note that in actual calculations performed within both first-principles and model tight binding approaches, broken bonds of edge carbon atoms are saturated with hydrogen atoms as a rule and the dangling bonds do not contribute to the density of states in the vicinity of the Fermi energy.

of ZRs independent of their width [106, 109]. (The zero gap in ZRs is of topological origin [110].) In particular, based on the projected band structure of graphene, the degeneracy of the highest valence band state and lowest conduction band state is expected to appear at the wavevectors $|k| = (2\pi/3a)$, where $a = 2.46$ Å is the length of the unit cell. However, the calculations showed that the degeneracy occurs at $|k| = \pi/a$ independent of the ribbon width, and the corresponding wavefunctions are localized at the ribbon edges. In the vicinity of the Fermi level a pair of bands exist within a region of $(2\pi/3a) < |k| < \pi/a$. They decay exponentially [108, 111] into the centre of ZR with a k-dependent decay constant $\lambda(k) = -(2/3a)\ln|2\cos(ka/2)|$, and this feature is also obtained by *ab initio* calculations. These edge-related bands are degenerate at the Fermi level and are practically dispersionless, i.e. flat. This in turn gives rise to a very large density of states at E_F, which opens the possibility of a transition to a magnetic phase. (Note that this cannot happen in two-dimensional infinite graphene, which has a vanishing density of states at the Fermi level.) The occurrence of spin polarization of graphene zigzag ribbons was first demonstrated by Fujita *et al* [111]. They used the Hubbard model and showed that even an infinitesimal on-site Coulomb repulsion induces a finite magnetization of edge atoms of about 0.2 μ_B. This result has been confirmed by subsequent first-principles studies [108, 112].

Inclusion of spin polarization of ZRs leads to the magnetic insulating ground state, with ferromagnetic order at each zigzag edge and an antiferromagnetic coupling between the edges. The bandgap between the spin-up and spin-down states is determined not only by exchange interactions but also by quantum confinement, and it decreases with increasing ZR width. Magnetic interaction energies at the edges are quite large. For example, in the case of 16-ZR the magnetic moment per edge atom is 0.43 μ_B and the energy difference between the spin-polarized and non-polarized configurations $\Delta E^{FM-PM} = 20$ meV/atom [113]. This energy is fairly independent of the ZR width. Comparable results (magnetic moment equal to 0.3 μ_B and ΔE^{FM-PM} of about 20 meV per edge atom) were obtained in [114]. On the other hand, the AFM interaction between spins on opposite edges decreases with the increasing width due to the relatively fast decay of magnetization away from an edge. In the case of a 16-ZR the coupling is about 2 meV/atom and it becomes vanishingly small for N_z larger than about 30 [113, 115]. A similar magnetic ground state was found for the ZRs without the hydrogen termination, but in this case the magnetic moment per atom is much larger, 1.28 μ_B [115]. Finally, the impact of the in-plane electric field perpendicular to the ZR axis was investigated [113]; the field-induced energy shifts at both edges close the gap for one orientation of spins, and open it for the opposite orientation. As a result, the system becomes half-metallic for sufficiently high fields, whose magnitude depends on the ribbon width (since this is the width which determines the bandgap). This result shows the interplay between electric field and electronic spin degree of freedom in systems based on graphene.

The calculated spatial distribution of spin density is shown in figure 6.2. Its shape follows from two effects. The first one is the fact that in the case of ZR the two sublattices of the graphene network are non-equivalent, and they differ by a staggered potential [116]. The sublattices have opposite spin polarizations, as seen in the figure, and this is why the spin arrangement at the edge is sometimes referred to as an antiferrimagnetic rather than a ferromagnetic one. The second factor is the exponential decay of the edge states, less visible in the figure because the ribbon is very narrow.

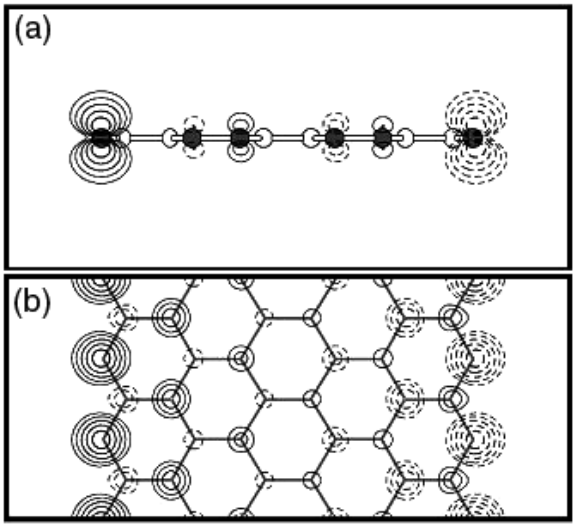

Figure 6.2. Contour plots of spin density (a) on a plane perpendicular to a ZR and (b) on a plane including the ribbon. In (a) the edges are perpendicular to the plane and C atoms on the plane are depicted by shaded circles. Positive and negative values of the spin density are shown by solid and dashed lines, respectively. Each contour represents twice (or half) the density of the adjacent contour lines. Reproduced with permission from [112]. Copyright 2001 by the American Physical Society.

Theoretical results summarized above hold for ideal ZRs. In reality, edges of nanographene are a mixture of zigzag and armchair types, they can have an orientation different from an ideal AN or ZN and they can contain a number of structural defects. The impact of these factors on the edge states was analysed, for example, in [98, 106, 117]. In particular, the presence of defects, such as an admixture of non-magnetic 'armchair defects', reduces the spin polarization and leads to its suppression at substantial defect concentrations [98]. This effect is illustrated in figure 6.3, which shows spin polarization of a misoriented ZR with a 'monolayer step'.

A second effect that can suppress spin polarization of ZRs is the presence of free carriers: the magnetization can be destroyed by the n-type or p-type carrier doping at sufficiently high concentrations [114]. Free carriers in graphene are indeed observed and are likely to be introduced during the preparation process. The observed concentrations of about 10^{13} cm^{-2} are sufficient to strongly reduce or even destroy both the magnetic moments of the edge atoms and the spin polarization.

Experimentally, atomic-scale morphology and electronic structure were investigated for ribbons and dots with 2–20 nm or larger lateral dimensions [100–105, 118–120] using transmission electron microscopy, STM and scanning tunnelling spectroscopy. Spin polarization—which is the main theme of this review—is not directly measured in

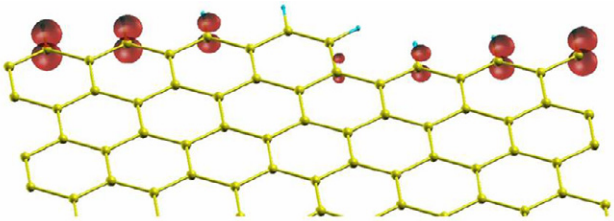

Figure 6.3. Isosurfaces of the electron density difference between the spin-up and spin-down densities in the misoriented ZR. Reproduced with permission from [98]. Copyright 2008 by the American Physical Society.

those experiments. However, tunnelling microscopy provides information about the local density of electron states and allows for a comparison of data with theoretical predictions. We recall that, according to theory, the main impact of the spin polarization of ZRs is to open the bandgap, thus driving the edge states from metallic to insulating and ferromagnetic. In qualitative agreement, transport measurements [103, 105, 121–123] reveal a semiconducting character of graphene dots and ribbons. The results of [105] suggest that the detailed edge structure plays a more important role than the overall crystallographic direction in determining the properties of the graphene nanoribbons. The dependence of the gap on the ribbon width was measured. The energy gap scales inversely with the ribbon width and follows theoretical predictions regarding the quantum confinement effects. Similarly, the study of [103] shows the dependence of the bandgap not only on the size but also on the termination of ribbons and dots. As pointed out in [98], spin polarization of ZRs leads to peaks in the local density of electronic states well above the Fermi energy. In the non-magnetic phase, peaks exist both below and above the Fermi level. These results can explain disagreements between the measurements performed by different groups [100, 104, 118], which study edges with different orientations and quality. Recently, energy gaps in ZR samples with ultrasmooth edges were observed [123], which indicates that spin polarization is non-vanishing. Finally [104] reports the results of scanning tunnelling microscopy and spectroscopy measurements of the local density of states near monoatomic steps of graphite surfaces. A clear peak in the local density of states at negative bias voltages was observed near the zigzag edges, while such a peak was not observed near the armchair edges. Although such edges are not equivalent to the edges of ZRs, the authors tentatively interpret this peak as the manifestation of the edge state of ZRs.

7. Summary and conclusions

Magnetism in systems without transition metal ions is an emerging subject in condensed matter physics. Most of the results reviewed here were obtained in the last decade and involve a large variety of systems. In a number of cases, research was initiated by theoretical calculations that predicted robust spin polarization of edges of nanoribbons, of ideal bulk II–V compounds or non-magnetic hosts with non-magnetic impurities. Several of those predictions are waiting for experimental confirmation. In other cases, in particular in various forms of carbon, such as carbon nanofoam or irradiated graphite, the experimental discoveries were unexpected and came first. Current theoretical understanding points out that spin polarization in the considered systems has a common physical origin, which is the high Hund energy of the p shells of light atoms from the second row of the periodic table (C, N and O), which persists in solids even after hybridization with neighbours and formation of bands.

The topic is open today and, in spite of the recent progress, presents challenges regarding all reviewed aspects. In particular, neither II–V nor II–IV compounds in the rock salt structure (section 2) were grown, and they are interesting even from the purely academic point of view. Molecular magnets reviewed in section 3 in turn are antiferromagnetic, thus less interesting from the point of view of applications. However, theoretical results obtained for those and other systems demonstrate that the problem of a correct treatment of correlations, traditionally reserved for heavy fermion systems, or in general d or f shell systems, may turn out to be decisive even in the case of carbon-based systems, nitrides and oxides, where the 2p shell plays a dominant role.

Section 4 is devoted to magnetism induced by defects and dopants. The room-temperature ferromagnetism observed for ZnO with C is now confirmed, but not controlled, and technological problems with the growth of high quality ZnO even without dopants suggest extending the studies to, for example, III-N nitrides. At this point it is difficult to propose which type of defects, intentional impurities or native defects such as vacancies, is a superior source of FM. On the one hand, high concentrations of dopants, exceeding 1 at.%, are easier to be controlled than a pronounced crystal non-stoichiometry. Second, equilibrium concentrations of vacancies are a few orders of magnitude too low to allow for FM. Third, irradiation of semiconductors typically generates vacancy–interstitial pairs that compensate each other, and thus partially occupied defect-induced bands are not expected to form. On the other hand, however, irradiation turned out to be efficient in the case of graphite, as pointed out in section 5. Functionalization of this or other ferromagnetic organic systems could lead to ‘organic magnetronics’, analogous to organic electronics which already found its place in applications. Given the ongoing research effort devoted to the reviewed issues including graphene, see section 6, the topic of this review is likely to attract attention in the near future.

Acknowledgments

Part of this work was done during the stay of PB at North Carolina State University in Raleigh. PB thanks J Bernhole for his hospitality, and for helpful discussions with him and with J Jiang and W Li. Work was partially supported by a grant from the Polish Ministry of Science and Higher Education NN 202 103036.

Note added in proof. After the submission of the paper we became aware of a paper pointing out sources of experimental errors in observations of nanoscale magnetism [124].

References

[1] Kukasabe K, Geshi M, Tsukamoto H and Suzuki N 2004 *J. Phys.: Condens. Matter* **16** S5639
[2] Volnianska O, Jakubas P and Bogusławski P 2006 *J. Alloys Compounds* **423** 191
[3] Sieberer M, Redinger J, Khmelevskyi S and Mohn P 2006 *Phys. Rev.* B **73** 024404
[4] Volnianska O and Bogusławski P 2007 *Phys. Rev.* B **75** 224418
[5] Geshi M, Kusakabe K, Nagara H and Suzuki N 2007 *Phys. Rev.* B **76** 054433
[6] Gao G Y, Yao K L, Şasioglu E, Sandratskii L M, Liu Z L and Jiang J L 2007 *Phys. Rev.* B **75** 174442
[7] Gao G Y and Yao K L 2007 *Appl. Phys. Lett.* **91** 082512
[8] Gao G Y, Yao K L, Liu Z L, Jiang J L, Yu L H and Shi Y L 2007 *J. Phys.: Condens. Matter* **19** 315222
[9] Li Y and Yu J 2008 *Phys. Rev.* B **78** 165203
[10] Yao K L, Jiang J L, Liu Z L and Gao G Y 2006 *Phys. Lett.* A **359** 326
[11] Peng H, Xiang H J, Wei S H, Li S S, Xia J B and Li J 2009 *Phys. Rev. Lett.* **102** 017201
[12] Djemia P *et al* 2004 *Acta Phys. Pol.* A **106** 239
[13] Gubanov V A, Liechtenstein A I and Postnikov A V 1992 *Magnetism and the Electronic Structure of Crystals* (Berlin: Springer)
[14] Takeuchi N 2002 *Phys. Rev.* B **65** 045204
[15] Meier R J and Helmholdt R B 1984 *Phys. Rev.* B **29** 1387
[16] Meier R J, Schinkel C J and de Visser A 1982 *J. Phys. C: Solid State Phys.* **15** 1015
[17] Akahama Y, Kawamura H, Häusermann D, Hanfland M and Shimomura O 1995 *Phys. Rev. Lett.* **74** 4690
[18] Shimizu K, Suhara K, Ikumo M, Eremets M I and Amaya K 1998 *Nature* **393** 767
[19] Labhart M, Raoux D, Känzig W and Bösch M A 1979 *Phys. Rev.* B **20** 53
[20] Attema J J, De Wijs G A, Blake G R and de Groot R A 2005 *J. Am. Chem. Soc.* **125** 16325
[21] Attema J J, De Wijs G A and de Groot R A 2007 *J. Phys.: Condens. Matter* **19** 165203
[22] Winterlik J, Fecher G H, Felser C, Mühle C and Jansen M 2007 *J. Am. Chem. Soc.* **129** 6990
[23] Jansen M, Hagenmayer R and Korber N 1999 *C. R. Acad. Sci. Ser.* 2c **2** 591
[24] Winterlik J *et al* 2009 *Phys. Rev.* B **79** 214410
[25] Winterlik J, Fecher G H, Jenkins C A, Felser C, Mühle C, Doll K, Jansen M, Sandratskii L M and Kübler J 2009 *Phys. Rev. Lett.* **102** 016401
[26] Kovacik R and Ederer C 2009 *Phys. Rev.* B **80** 140411(R)
[27] Auffermann G, Prots Y and Kniep R 2001 *Angew. Chem. Int. Edn* **40** 547
[28] Auffermann G, Schmidt U, Bayer B, Prots Yu and Kniep R 2002 *Anal. Bioanal. Chem.* **373** 880
[29] Volnianska O and Boguslawski P 2008 *Phys. Rev.* B **77** 220403(R)
[30] Galland D and Herve A 1970 *Phys. Lett.* **33** A1
[31] Evans S M, Giles N C, Halliburton L E and Kappers L A 2008 *J. Appl. Phys.* **103** 043710
[32] Vlasenko L S and Watkins G D 2005 *Phys. Rev.* B **72** 035203
[33] Halliburton L E, Cowan D L, Blake W B J and Wertz J E 1973 *Phys. Rev.* B **8** 1610
[34] Rose B H and Halliburton L E 1974 *J. Phys. C: Solid State Phys.* **7** 3981
[35] Kennedy T A, Wilsey N D, Krebs J J and Stauss G H 1983 *Phys. Rev. Lett.* **50** 1281
[36] Itoh H, Kawasuso A, Ohshima T, Yoshikawa M, Nashiyama I, Tanigawa S, Misawa S, Okumura H and Yoshida S 1997 *Phys. Status Solidi* a **162** 173
[37] Mizuochi N 2005 *Phys. Rev.* B **72** 235208
[38] Torpo L, Nieminen R M, Laasonen K E and Poykko S 1999 *Appl. Phys. Lett.* **74** 221
[39] Wimbauer T, Meyer B K, Hofstaetter A, Scharmann A and Overhof H 1997 *Phys. Rev.* B **56** 7384
[40] Zywietz A, Furthmüller J and Bechstedt F 1999 *Phys. Rev.* B **59** 15166
[41] Lento J, Pesola M, Mozos J L and Nieminen R M 2000 *Appl. Phys. Lett.* **77** 232
[42] Elfimov I S, Yunoki S and Sawatzky G A 2002 *Phys. Rev. Lett.* **89** 216403
[43] Osorio-Guillen J, Lany S, Barabash S V and Zunger A 2006 *Phys. Rev. Lett.* **96** 107203
[44] Pemmaraju C D and Sanvito S 2005 *Phys. Rev. Lett.* **94** 217205
[45] Osorio-Guillén J, Lany S, Barabash S V and Zunger A 2007 *Phys. Rev.* B **75** 184421
[46] Mahadevan P and Mahalakshmi S 2006 *Phys. Rev.* B **73** 153201
[47] Volnianska O 2009 *PhD Thesis* Institute of Physics PAN, Warsaw
[48] Dev P, Xue Y and Zhang P 2008 *Phys. Rev. Lett.* **100** 117204
[49] Drogetti A, Pemmaraju C D and Sanvito S 2008 *Phys. Rev.* B **78** 140404(R)
[50] Wang F, Pang Z, Lin L, Fang S, Dai Y and Han S 2009 *Phys. Rev.* B **80** 144424
[51] Chanier T, Opahle I, Sargolzaei M, Hayn R and Lannoo M 2008 *Phys. Rev. Lett.* **100** 026405
[52] Chan J A, Lany S and Zunger A 2009 *Phys. Rev. Lett.* **103** 016404
[53] Bouzerar G and Ziman T 2006 *Phys. Rev. Lett.* **96** 207602
[54] Boguslawski P, Briggs E and Bernholc J 1995 *Phys. Rev.* B **51** 17255 (R)
[55] Pan H, Yi J B, Shen L, Wu R Q, Yang J H, Lin J Y, Feng Y P, Ding J, Van L H and Yin J H 2007 *Phys. Rev. Lett.* **99** 127201
[56] Herng T S, Lau S P, Wei C S, Wang L, Zhao B C, Tanemura M and Akaike Y 2009 *Appl. Phys. Lett.* **95** 133103
[57] Herng T S, Lau S P, Wang L, Zhao B C, Yu S F, Tanemura M, Akaike A and Teng K S 2009 *Appl. Phys. Lett.* **95** 012505
[58] Boguslawski P and Bernholc J 1996 *Appl. Phys. Lett.* **69** 233
[59] Ye X J, Song H A, Zhong W, Xu M H, Qi X S, Jin C Q, Yang Z X, Au C T and Du Y W 2008 *J. Phys. D: Appl. Phys.* **41** 155005
[60] Yu C F, Lin T J, Sun S-J and Chou H 2007 *J. Phys. D: Appl. Phys.* **40** 6497
[61] Elfimov I S, Rusydi A, Csiszar S I, Hu Z, Hsieh H H, Lin H J, Chen C T, Liang R and Sawatzky G A 2007 *Phys. Rev. Lett.* **98** 137202
[62] Kenmochi K, Seike M, Sato K, Yanase A and Katayama-Yoshida H 2005 *Japan. J. Appl. Phys.* **44** L51
[63] Maca F, Kudrnovský J, Drchal V and Bouzerar G 2008 *Appl. Phys. Lett.* **92** 212503
[64] Kenmochi K, Dinh V A, Sato K, Yanase A and Katayama-Yoshida H 2004 *J. Phys. Soc. Japan* **73** 2952
[65] Shen L, Wu R Q, Pan H, Peng G W, Yang M, Sha Z D and Feng Y P 2008 *Phys. Rev.* B **78** 073306
[66] Maropoulos P, Lezaic M and Blugel S 2009 *Phys. Rev.* B **80** 184403
[67] Pardo V and Pickett W E 2008 *Phys. Rev.* B **78** 134427
[68] Lathiotakis N N, Andriotis A N and Menon M 2008 *Phys. Rev.* B **78** 193311
[69] Blundell S J and Pratt F L 2004 *J. Phys.: Condens. Matter* **16** R771
[70] Turek P, Nozawa K, Shiomi D, Awaga K, Inabe T, Maruyama Y and Kinoshita M 1991 *Chem. Phys. Lett.* **180** 327
[71] Makarova T L, Sundquist B, Hohne R, Esquinazi P, Kopelevich Y, Scharff P, Davidov V A, Kashevarova L S and Rakhmanina A V 2001 *Nature* **413** 716

Makarova T L, Sundquist B, Hohne R, Esquinazi P, Kopelevich Y, Scharff P, Davidov V A, Kashevarova L S and Rakhmanina A V 2006 *Nature* **440** 707 (retraction)
[72] Wood R A, Lewis M H, Lees M R, Bennington S M, Cain M G and Kitamura N 2002 *J. Phys.: Condens. Matter* **14** L385
[73] Narymbetov B, Omerzu A, Kabanov V V, Tokumoto M, Kobayashi H and Michailovic D 2000 *Nature* **407** 883
[74] Simon F *et al* 2006 *Phys. Rev. Lett.* **97** 136801
[75] Zhao J, Zeng C, Cheng X, Wang K, Wang G, Yang J, Hou J G and Zhu Q 2005 *Phys. Rev. Lett.* **95** 045502
[76] Hearneit W, Boehme C, Schaefer S, Huebener K, Fostiropoulos K and Lips L 2007 *Phys. Rev. Lett.* **98** 216601
[77] Yang C-K 2008 *Appl. Phys. Lett.* **92** 033103
[78] Parkansky N, Alterkop B, Boxman R L, Leitus G, Berkh O, Barkay Z, Rosenberg Yu and Eliaz N 2008 *Carbon* **46** 215
[79] Shibayama Y, Sato H, Enoki T and Endo M 2000 *Phys. Rev. Lett.* **84** 1744
[80] Rode A V, Gamaly E G, Christy A G, Fitz Gerald J G, Hyde S T, Elliman R G, Luther-Davies B, Veinger A I, Androulakis J and Giapintzakis J 2004 *Phys. Rev.* B **70** 054407
[81] Esquinazi P, Setzer A, Hohne R, Semmelhack C, Kopelevich Y, Spemann D, Butz T, Kohlstrunk B and Losche M 2002 *Phys. Rev.* B **66** 024429
[82] Esquinazi P, Spemann D, Hohne R, Setzer A, Han K-H and Butz T 2003 *Phys. Rev. Lett.* **91** 227201
[83] Ohldag H, Tyliszczak T, Hohne R, Spemann D, Esquinazi P, Ungureanu M and Butz T 2007 *Phys. Rev. Lett.* **98** 187204
[84] Talapatra S, Ganesan P G, Kim T, Vajtai R, Huang M, Shima M, Ramanath G, Srivastava D, Deevi S C and Ajayan P M 2005 *Phys. Rev. Lett.* **95** 97201
[85] Lehtinen P O, Foster A S, Ma Y, Krasheninnikov A V and Nieminen R M 2004 *Phys. Rev. Lett.* **93** 187202
[86] Lehtinen P O, Krasheninnikov A V, Foster A S and Nieminen R M 2006 *Carbon-Based Magnetism* ed T Makarova and F Palacio (Amsterdam: Elsevier) p 371
[87] Zhang Y, Talapatra S, Kar S, Vajtai R, Nayak S K and Ajayan P M 2007 *Phys. Rev. Lett.* **99** 107201
[88] El-Barbary A A, Telling R H, Ewels C P, Heggie M I and Briddon P R 2003 *Phys. Rev.* B **68** 144107
[89] Mombrú A W, Pardo H, Faccio R, de Lima O F, Leite E R, Zanelatto G, Lanfredi A J C, Cardoso C A and Araújo-Moreira F M 2005 *Phys. Rev.* B **71** 100404
[90] Červenka J, Katsnelson M I and Flipse C F J 2009 *Nat. Phys.* **5** 840
[91] Červenka J and Flipse C F J 2009 *Phys. Rev.* B **79** 195429
[92] Dresselhaus G, Dresselhaus G and Eklund P C 1996 *Science of Fullerenes and Carbon Nanotubes: Their Properties and Applications* (New York: Academic)
[93] McEuen P L, Fuhrer M S and Park H 2002 *IEEE Trans. Nanotechnol.* **1** 78
[94] See e.g., Wakabayashi K 2006 *Carbon Based Magnetism* ed T Makarova and F Palacio (New York: Elsevier) chapter 12
Katsnelson M I 2007 *Mater. Today* **10** 20
Geim A K 2009 *Science* **324** 1530
[95] Wallace P R 1947 *Phys. Rev.* **71** 622
[96] Ando T 2005 *J. Phys. Soc. Japan* **74** 777
[97] Castro Neto A H, Guinea F, Peres N M R, Novoselov K S and Geim A K 2009 *Rev. Mod. Phys.* **81** 109
[98] Jiang J, Lu W and Bernholc J 2008 *Phys. Rev. Lett.* **101** 246803
[99] Koskinen P, Malola S and Häkkinen H 2008 *Phys. Rev. Lett.* **101** 115502
[100] Kobayashi Y, Fukui K, Enoki T, Kusakabe K and Kaburagi Y 2005 *Phys. Rev.* B **71** 193406
[101] Kobayashi Y, Fukui K, Enoki T and Kusakabe K 2006 *Phys. Rev.* B **73** 125415
[102] Girit C O *et al* 2009 *Science* **323** 1705
[103] Ritter K A and Lyding J W 2009 *Nat. Mater.* **8** 235
[104] Niimi Y, Matsui T, Kambara H, Tagami K, Tsukada M and Fukuyama H 2006 *Phys. Rev.* B **73** 085421
[105] Han M Y, Özyilmaz B, Zhang Y and Kim P 2007 *Phys. Rev. Lett.* **98** 206805
[106] Nakada K, Fujita M, Dresselhaus G and Dresselhaus M S 1996 *Phys. Rev.* B **54** 17954
[107] Brey L and Fertig H A 2006 *Phys. Rev.* B **73** 235411
[108] Son Y-W, Cohen M L and Louie S G 2006 *Phys. Rev. Lett.* **97** 216803
[109] Wakabayashi K, Fujita M, Ajiki H and Sigrist M 1999 *Phys. Rev.* B **59** 8271
[110] Ryu S and Hatsugai Y 2002 *Phys. Rev. Lett.* **89** 077002
[111] Fujita M, Wakabayashi K, Nakata K and Kusakabe K 1996 *J. Phys. Soc. Japan* **65** 1920
[112] Okada S and Oshiyama A 2001 *Phys. Rev. Lett.* **87** 146803
[113] Son Y-W, Cohen M L and Louie S G 2006 *Nature* **444** 347
[114] Wu F, Kan E, Xiang H, Wei S-H, Whangbo M-H and Yang J 2009 *Appl. Phys. Lett.* **94** 223105
[115] Lee H, Son Y-W, Park N, Han S and Yu J 2005 *Phys. Rev.* B **72** 174431
[116] Kane C L and Mele E J 2005 *Phys. Rev. Lett.* **95** 146802
[117] Ezawa M 2006 *Phys. Rev.* B **73** 045432
[118] Klusek Z, Waqar Z, Denisov E A, Kompaniets T N, Makarenko I V, Titkov A N and Bhatti A S 2000 *Appl. Surf. Sci.* **161** 508
[119] Novoselov K S, Geim A K, Morozov S V, Jiang D, Katsnelson M I, Grigorieva I V, Dubonos S V and Firsov A A 2005 *Nature* **438** 197
[120] Meyer J C, Geim A K, Katsnelson M I, Novoselov K S, Booth T J and Roth S 2007 *Nature* **446** 60
[121] Chen Z, Lin Y M, Rooks M and Avouris P 2007 *Physica* E **40** 228
[122] Ponomarenko L A, Schedin F, Katsnelson M I, Yang R, Hill E W, Novoselov K S and Geim A K 2008 *Science* **320** 356
[123] Li X, Wang X, Zhang L, Lee S and Dai H 2008 *Science* **319** 1229
[124] Garcia M A *et al* 2009 *J. Appl. Phys.* **105** 013925